

pubs.acs.org/estengg Article

Demonstration of Hollow Fiber Membrane-Based Enclosed Space Air Remediation for Capture of an Aerosolized Synthetic SARS-CoV-2 Mimic and Pseudovirus Particles

Kevin C. Baldridge, Kearstin Edmonds, Thomas Dziubla, J. Zach Hilt, Rebecca E. Dutch, and Dibakar Bhattacharyya*



Cite This: https://doi.org/10.1021/acsestengg.1c00369



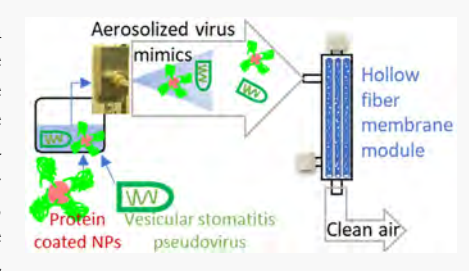
ACCESS I

III Metrics & More

Article Recommendations

Supporting Information

ABSTRACT: Reduction of airborne viral particles in enclosed spaces is critical in controlling pandemics. Three different hollow fiber membrane (HFM) modules were investigated for viral aerosol separation in enclosed spaces. Pore structures were characterized by scanning electron microscopy, and air transport properties were measured. Particle removal efficiency was characterized using aerosols generated by a collision atomizer from a defined mixture of synthetic nanoparticles including SARS-CoV-2 mimics (protein-coated 100 nm polystyrene). HFM1 (polyvinylidene fluoride, \sim 50–1300 nm pores) demonstrated 96.5–100% efficiency for aerosols in the size range of 0.3–3 μ m at a flow rate of 18.6 \pm 0.3 SLPM (\sim 1650 LMH), whereas HFM2



(polypropylene, \sim 40 nm pores) and HFM3 (hydrophilized polyether sulfone, \sim 140–750 nm pores) demonstrated 99.65–100% and 98.8–100% efficiency at flow rates of 19.7 \pm 0.3 SLPM (\sim 820 LMH) and 19.4 \pm 0.2 SLPM (\sim 4455 LMH), respectively. Additionally, lasting filtration with minimal fouling was demonstrated using ambient aerosols over 2 days. Finally, each module was evaluated with pseudovirus (vesicular stomatitis virus) aerosol, demonstrating 99.3% (HFM1), >99.8% (HFM2), and >99.8% (HFM3) reduction in active pseudovirus titer as a direct measure of viral particle removal. These results quantified the aerosol separation efficiency of HFMs and highlight the need for further development of this technology to aid the fight against airborne viruses and particulate matter concerning human health.

KEYWORDS: PM2.5, SARS-CoV-2, COVID-19, indoor air, bioaerosol

INTRODUCTION

The key role of airborne transmission of COVID-19 in the rapid expansion and widespread nature of the current pandemic has highlighted the need for highly effective, low pressure filter technologies to remove viral aerosols in indoor environments like restaurants^{1,2} and hospitals.³⁻⁶ The emergence of more transmissible viruses like the Delta variant further emphasizes the value of controlling respiratory spread. Viral aerosols (droplets $<5 \mu m$) are created by medical procedures, eating, coughing, sneezing, and even normal breathing, 8-11 and these aerosols as well as larger droplets contribute to viral transmission. Aerosols containing pathogens like SARS-CoV-2 have been identified in a number of studies (reviewed in ref 9), further establishing the need for costeffective and efficient air purification technologies in this and future respiratory pandemics. In addition to bioaerosols, there is a great need for effective technologies to remove particulate pollution from air given the known detrimental health effects of exposure to particulate matter. 12-15 Furthermore, it has been suggested that PM_{2.5} (airborne particulate matter generally 2.5 μ m or smaller) may act as a carrier for transmission of viral aerosols 16 and even that PM_{2.5} exposure increases the risk of severe COVID-19, 17,18 reaffirming the

need of aerosol filtration in mitigating the spread of airborne pathogens as well as protecting human health from various airborne particulate matter.

Porous, thin membranes with asymmetric pore structure offer several features that may be advantageous for aerosol filtration.¹⁹ Polymer materials can be easily modified for surface functionalization to tune surface properties of the membrane or add a new functionality such as enzymes or nanoparticles.^{20–22} Easy control of thickness, pore size and structure, and porosity allows for tuning the size cutoff for a given application, i.e., filtration of viruses with defined size, by controlling transport properties to minimize the pressure drop while maintaining high efficiency filtration. The wide range of tunable features may provide significant advantages. Asymmetric pore structures, for example, can provide highly efficient filtration (via sieving) with small pore sizes at the feed surface,

Received: October 7, 2021
Revised: December 22, 2021
Accepted: December 28, 2021



while minimizing the pressure drop with widening pore structure below (Figure 1A). In this orientation, fouling may

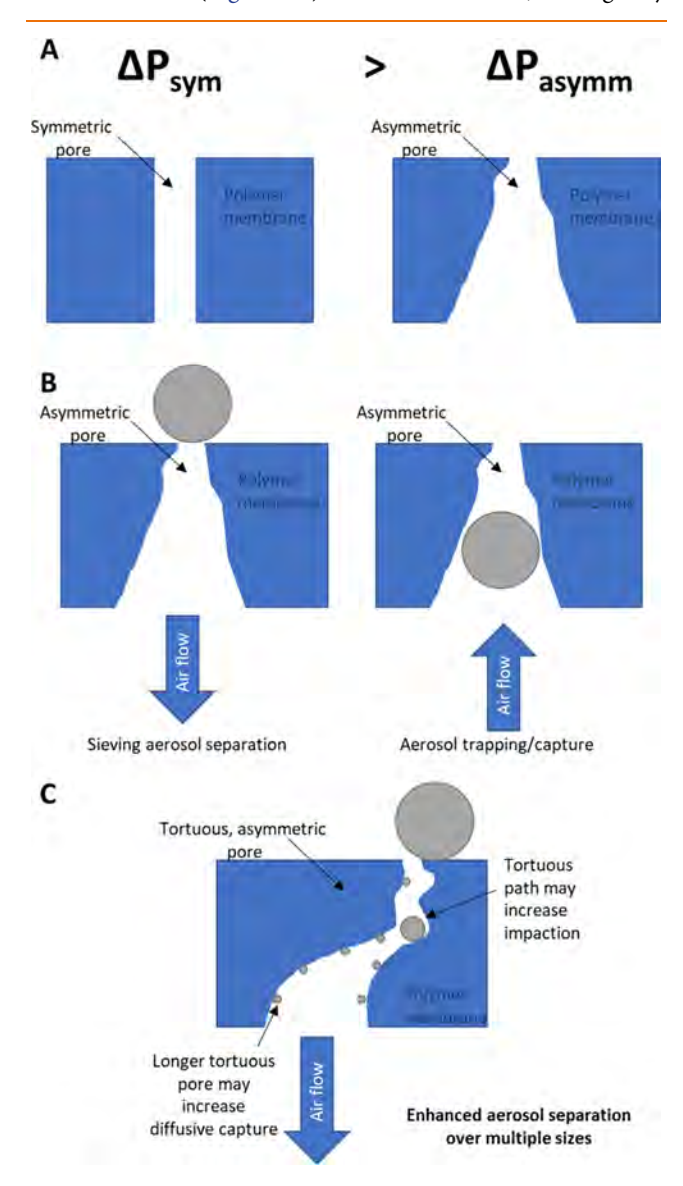


Figure 1. Schematic representation of pore structure role in aerosol filtration. (A) Asymmetric pores can minimize pressure drop while maintaining a small effective pore size for high efficiency separation. (B) The mechanism of separation can be controlled by controlling the direction of air flow through asymmetric pores to reject or capture particles within the membrane. (C) Tortuous pathways in the membrane pores could enhance aerosol separation over multiple size ranges by increasing diffusion and/or impaction.

be minimized by the sieving separation mechanism since particles are unable to enter the filter media and clog air transport pathways (Figure 1B). Moreover, the mechanism of aerosol separation can be tuned by changing the configuration of air flow through an asymmetric membrane, i.e., sieving separation at the porous membrane surface in one direction versus capture within the porous structure in the other (Figure 1B,C). The ability to capture particles within the porous network may also have potential advantages for sensing and quantifying certain captured components of interest such as pollutants ²³ or pathogens. ²⁴

Hollow fiber membranes (HFMs) are a particular type of membrane with cylindrical geometry where transport occurs across the membrane in the radial direction. HFMs are highly advantageous for high-throughput scenarios since their geometry allows for high surface area to volume ratio, packing large filtration areas into a small footprint, and for low pressure operations. Due to these advantages, HFMs have been applied extensively in the water purification and membrane distillation areas where a high surface area is needed to account for the low flux through highly selective membranes like those used in reverse osmosis²⁵ or membrane distillation. ^{26–28}

Only a few studies have investigated the use of HFMs for aerosol filtration; however, these have shown great promise for separating PM_{2.5} from air. Several studies have demonstrated efficient aerosol filtration with hollow fiber membranes, 29-36 often with combustion products as the test aerosol similar to the biomass burning-derived secondary organic aerosols (SOA), which are a major contributor to anthropogenic $PM_{2.5}$. Furthermore, some have shown easy regeneration/reuse of HFMs in filtering aerosols. To our knowledge, no studies have demonstrated viral aerosol capture using HFM modules with differing properties. Efforts to design filters and methods for removing/deactivating viral aerosols have increased in light of the current coronavirus pandemic.^{38–44} We sought to use commercially available HFMs (polypropylene, PVDF, and polyether sulfone) for quickly deployable and effective aerosol filtration to curb the spread of the COVID-19 pandemic rather than developing new membranes or other novel solutions that will take time to reach the public.

In this work, the overall objective was to quantify air and particle transport in commercially available HFM modules for air filtration to remove viral aerosols and other airborne particles as a quickly deployable and cheaper alternative to HEPA systems with higher aerosol removal efficiency than standard HVAC filtration. Two commercial membranes and one noncommercial production-scale membrane were chosen with varying characteristics (pore size, shape, and asymmetry; membrane thickness; material hydrophobicity; and module design) to establish relationships between membrane features and aerosol filtration functionality. Membranes from these modules were characterized by porosimetry and scanning electron microscopy. The modules' effective filtration of aerosol mixtures of controlled sizes, including protein-labeled nanoparticle mimics of SARS-CoV-2, was confirmed. The realworld applicability for each module was evaluated by longer term (two day) filtration experiments with ambient aerosols. Finally, the HFM modules were evaluated with aerosolized vesicular stomatitis pseudovirus particles with filtration efficiency characterized by viral titering assays, demonstrating their value for reducing airborne respiratory illness spread.

■ MATERIALS AND METHODS

Aerosol Testing System Construction. The membrane-based aerosol testing system was constructed as shown in Supporting Information Figure 1. Tubing was mostly constructed of PTFE 1/2 in. O.D. tubing (McMaster Carr) with some exceptions noted in the schematic. All connections and valves were brass or stainless steel (Mcmaster Carr). Aerosol size distributions were measured in an ~ 3 in. I.D. PTFE tube (constructed of a rolled and taped skived PTFE sheet from Mcmaster Carr) that served as a depressurizing chamber to avoid pressure damage to the pump in the optical particle counter (MetOne Instruments GT526S). Mass flow

Table 1. Summary of Properties Collected for Hollow Fiber Membrane Modules Tested in This Work

	HFM1	HFM2	HFM3
membrane material	polyvinylidene fluoride (PVDF) (hydrophobic)	polypropylene (PP) (hydrophobic)	hydrophilized polyether sulfone (hPES) (hydrophilic)
module packing fraction ^a	0.34	0.47	0.48
mean pore size ^a	1153 nm (mercury porosimetry)	40 nm (manufacturer)	200 nm (manufacturer)
		38 nm (N2 porosimetry)	
shell surface mean pore size ^a	$57 \pm 35 \text{ nm}$	$42 \pm 17 \text{ nm}$	$140 \pm 87 \text{ nm}$
lumen surface mean pore size ^a	$1346 \pm 1086 \text{ nm}$	$46 \pm 27 \text{ nm}$	$748 \pm 896 \text{ nm}$
bulk porosity ^a	24% (Hg porosimetry)	24% (N ₂ porosimetry)	45% (SEM cross-section pore analysis)
		40% (manufacturer)	
tortuosity ^a	3.1692 (Hg porosimetry)	not measured	not measured
thickness ^a	$412.6 \pm 106.2 \ \mu \text{m}$	$41.8 \pm 2.2 \ \mu m$	$85.5 \pm 3.5 \ \mu m$

rates were measured by a thermal mass flow meter (Model 4043, TSI), and the transmembrane pressure differential was measured using a digital manometer (0–100 psi, SPER Scientific).

Membrane Structural Characterization. The module packing fraction was estimated as the ratio of the fiber count times fiber cross-sectional area divided by shell cross-sectional area. Hollow fiber membrane samples (including tribore HF) were prepared for scanning electron microscopy by mounting on EM conductive carbon tape (Nisshin) and (in most cases) sputter coating with 5 nm platinum (Leica EM ACE600). Imaging was performed in the University of Kentucky Electron Microscopy Center using FEI Helios Scanning Electron Microscope (SEM). Detailed preparation methods for each sample are provided in Supporting Information Detailed Methods. Nitrogen porosimetry (Micromeritics Tristar 3000) was also performed for HFM2 to validate other measurements determined by SEM (Table 1).

Air Permeability Characterization. For all permeability experiments, the air was supplied from a filtered regulator set at ~4.1 bar attached at two building air outlets, with feed pressure further controlled by the needle valves at each outlet. The filtered air generally has a baseline residual level of particles of ~300 per liter for 300–500 nm particles. For air permeability experiments, the setup in Supporting Information Figure 1 was modified to take the atomizer out of the system. The needle valves at the filter regulators were used to control the pressure drop across the module, and the air flow rates, temperatures, and pressure drop readings were recorded. The measured mass flow rates were then normalized by total surface area of the module, as estimated by methods detailed in Supporting Information Detailed Methods.

Filtration Efficiency Assessment. Aerosols were generated using a constant output collision atomizer (TSI model 3076) fed from a mixture of 50 nm lipoic acid-coated gold nanoparticles (Nanocomposix), protein-labeled (10:1 GFP:Spike) 100 nm COOH-functionalized polystyrene latex nanoparticles (Bangs Laboratories, Inc), and 500 nm aminefunctionalized polystyrene latex nanoparticles (Polysciences). The mixture was characterized via dynamic light scattering (Anton Paar Litesizer 500) before each aerosol experiment (Supporting Information Figure 2). The protein-labeled 100 nm PSL nanoparticles were prepared by first coating particles with Ni²⁺ followed by labeling with either a superfolder green fluorescent protein (GFP) or a spike protein with polyhistidine tags, with labeling verified by a change in hydrodynamic

diameter measured by DLS and stability of immobilization later confirmed by Bradford and SDS-PAGE analyses; unfortunately, the spike protein was found to be degraded after several months of storage, and therefore we can only confirm that 90% of the 100 nm particles were protein-labeled with a GFP (Supporting Information Figure 3). Detailed methods can be found in the Supporting Information. Aerosol concentrations were measured using an optical particle counter (Met One Instruments GT-526S), operated in differential mode to show individual totals for each default size bin (0.3- $0.5 \mu \text{m}$, $0.5-0.7 \mu \text{m}$, $0.7-1 \mu \text{m}$, $1-2 \mu \text{m}$, $2-3 \mu \text{m}$, $>3 \mu \text{m}$). At each time point data were collected by first measuring the aerosol concentrations and then switching the outlet to the flow meter for pressure drop/flow rate measurement. Next, the bypass valve was switched to circumvent the filter, and the pressure drop/flow rate measurement was taken before switching the outlet valve back to the sampling tube. The unfiltered stream flushed the sampling tube for 1−3 min before taking the unfiltered aerosol concentration measurement $(C_{\text{unfiltered}})$. Thus, matching unfiltered/filtered concentrations are available for each time point, as well as pressure drop (ΔP) and flow rate data for each. Filtration efficiency was calculated as a percentage by eq 1, and the quality factor was calculated by eq 2:

$$\eta = \frac{C_{\text{unfiltered}} - C_{\text{filtered}}}{C_{\text{unfiltered}}} \times 100$$
 (1)

$$QF = \frac{-\ln(1 - \frac{\eta}{100})}{\Delta P} \tag{2}$$

For long-term filtration studies, the system was operated with a vacuum pump driving filtration of ambient aerosols, with the system set up as shown in Supporting Information Figure 4. In this case, a Grimm miniWRAS 1371 aerosol spectrometer was used to characterize particle size distributions, which provides size distribution and concentration information for particle diameters from 10 nm to 193 nm using an electrophoretic mobility sizer with electrometric detection and from 253 nm to 35 μ m using an optical scattering detector. Occasional outliers in measurements of particle counts were identified as >3 standard deviations from the mean over the measurement time range for each filtered and unfiltered point, and uncertainty was propagated to the value of efficiency calculated from the corresponding time-averaged counts.

Pseudovirus Production. The purification process is depicted in Supporting Information Figure 5. HEK 293T cells

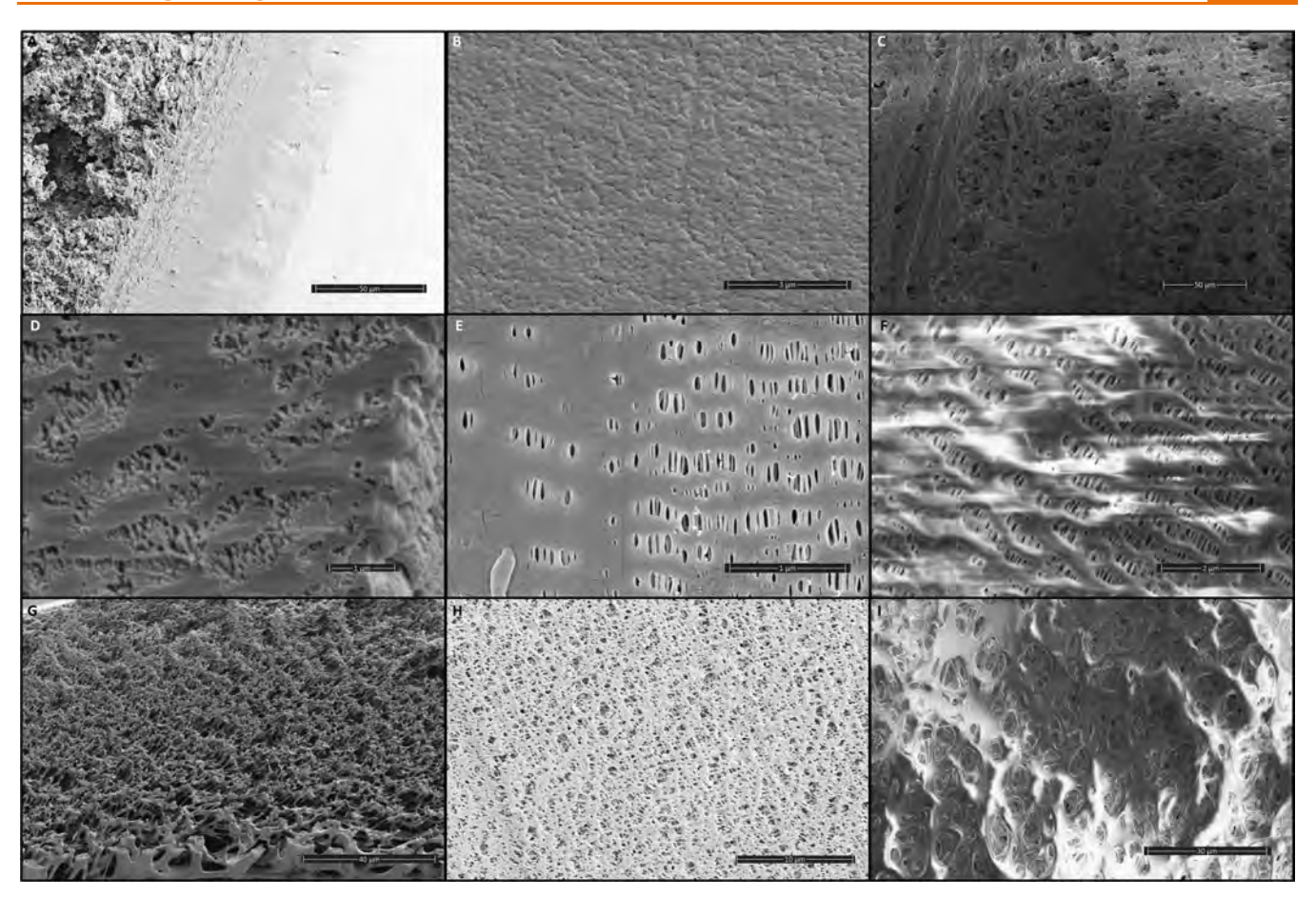


Figure 2. Comparison of hollow fiber membranes by SEM imaging. Cross-section images of each membrane demonstrate the asymmetric pore structures in (A) HFM1 and (G) HFM3 and symmetric pores in (D) HFM2. HFM1 demonstrates highly asymmetric pore structure, with (B) small <100 nm pores at the shell surface and (C) larger pore openings >1 μ m at the lumen surface. In contrast, HFM2 has highly symmetric pores <100 nm at both (E) the shell and (F) the lumen surfaces. HFM3 has a moderately asymmetric structure, with (H) small ~140 nm pores at the shell surface and (I) wider ~750 nm pores at the lumen surface.

were cultured in DMEM + 10% FBS. Transfections of 293T cells, with VSV G protein, took place in 10 cm dishes, with 8 μg of plasmid DNA, using Lipofectamine 3000 reagents (Life Technologies L3000075), and incubated for 24 h at 37 °C and 5% CO₂. Cells were then transduced with VSV Δ G-GFP genome pseudovirus, incubated for 1 h, washed 2× with phosphate buffered saline (PBS), and incubated for 24 h. Supernatants were collected, frozen in a dry ice methanol bath, and stored at -80 °C. Samples were purified on a 20% sucrose cushion in ultracentrifuge rotor SW28, for 2 h at 27 000 rpm and 4 °C. Pseudovirus was resuspended in 10% sucrose in 1× TNE (50 mM Tris-HCL, 150 mM NaCl, and 1 mM EDTA), rocking at 4 °C overnight. Pseudovirus was pooled, frozen using a dry ice methanol bath, and stored at -80 °C.

Pseudovirus Aerosol Filtration Testing. For aerosol filtration, the system was prepared by disassembling and rinsing all tubing and fittings with 70% ethanol and reassembling it in a laminar flow biological safety cabinet, as shown in Supporting Information Figure 6 without the temperature and pressure probes. Additionally, the atomizer was sterilized by running 70% ethanol through it from a syringe. An initial experiment was conducted to determine the most efficient method for recapturing aerosolized pseudovirus, with the conclusion that bubbling through media was the best approach (Supporting Information Figure 7).

Pseudovirus stocks were thawed and diluted to 1:2 into HyClone Dulbecco's Modified Eagle Medium (DMEM) and then placed on ice during transport. The pseudovirus stock was loaded into a syringe, and the pump was set for 0.1 mL/min, consistent with the expected feed rate for the atomizer in recirculation mode that was used for nonbiological filtration tests. Aerosols were collected by a custom-made impinger comprised of a cell culture flask with 5 mL DMEM (Cytiva, cat. no. sh30022.01) and a serological pipet as a nozzle (Supporting Information Figure 8). After 5 min (delivery of 0.5 mL of pseudovirus solution, $\sim 2.7 \times 10^7$ particles), the pump turned off, and the air supplies were left on for 1-2 min to flush remaining aerosolized pseudoviruses through the filter and system; then, the air supplies were also turned off. The described method was used for each HFM, and a piece of PTFE tubing of equivalent length was used in place of any HFM test module for the control. Collected aerosols for each HFM and control were concentrated by centrifugation at 3260g and 4 °C for 4 min using a 100 kDa MWCO centrifugal ultrafiltration cassette (Pall) and tested by pseudovirus transduction assays.

Pseudovirus Transduction Assay. Stable ACE2 expressing HEK 293T cells were seeded in 24-well plates and transduced the following day with pseudovirus. Serial 10-fold dilutions were performed in a fresh 24-well plate, starting with 5 μ L of pseudovirus in DMEM+10% FBS, and 300 μ L per well

was transferred to an aspirated well of stable ACE2 293T cells. Transductions were incubated for 24 h, before being visualized on the Axiovert 200 M 5× objective fluorescent channel. Transduced (GFP-expressing) cells were counted, and the pseudoviral titer was calculated using the dilution factor. Samples were transduced in duplicate and were generally highly reproducible between technical replicates and independent biological experiments (see Supporting Information Figure 9).

Statistical analysis was carried out in R Studio⁴⁵ (code available upon request). A one-way ANOVA identified statistical differences (p < 0.01) among the group of four samples (unfiltered control, HFM1, HFM2, HFM3), as represented by the mean titer value of each biological experiment (N = 3), scaled to the undiluted starting titer for each experiment to account for variations in the starting titer for each experiment. Posthoc analysis was performed with Tukey's Honest Significant Difference test comparing each group using the same scaled titer values, with the resulting statistical significance cutoffs shown in Figure 7.

■ RESULTS AND DISCUSSION

In this study, the objective was to establish hollow fiber membrane modules with various structural and design features and polymer types as viral aerosol filters to reduce the airborne spread of pathogens. A schematic summary of this study is shown in Supporting Information Figure 10. We first establish predictive models (with comparison to experimental measurements) of air transport properties for each HFM. Next, we demonstrate efficient separation of synthetic (polystyrene and gold) aerosols of various sizes (including SARS-CoV-2 mimicking 100 nm polystyrene nanoparticles with protein surface coating). We demonstrate real-world applicability for HFMs by performing long-term filtration studies with ambient aerosols showing minimal pressure drop changes over time. Finally, we connect the observed separation of synthetic virus mimics with functional tests of pseudovirus removal via infectivity assays, confirming that HFMs are viable for enclosed space air filtration to help reduce the spread of airborne respiratory illnesses. To our knowledge, this work represents the first demonstration of hollow fiber membranes for viral aerosol filtration.

Selection of Hollow Fiber Membranes. In this work, three hollow fiber membranes (HFM1, tribore fibers from START Centre Singapore; HFM2, X50 membrane from 3M; and HFM3, Lifestraw from Vestergaard) were chosen for characterization and quantification as aerosol filters. These membranes have quite variable properties, from surface characteristics to pore size and uniformity. HFM1 has a highly asymmetric, larger pore structure that is spongy and open on the lumen side with smaller pores and denser structure on the shell side (Figure 2B,C, Table 1, Supporting Information Figures 11-13) and also has a unique tribore geometry (Supporting Information Figure 12) that may allow for higher diffusive capture due to increased surface area and higher pressure (i.e., more air processing capability) due to increased mechanical strength. On the other hand, HFM2 has more uniform surface pore structures (about 40 nm diameter) with porosity and pore sizes matching much more closely for the shell and lumen side (Table 1, Figure 2E,F, Supporting Information Figures 14-16). In addition to the more symmetric structure across the membrane thickness, this membrane has internal pore networks that are more fibrous

than spongy (Figure 2D, Supporting Information Figure 15), which may be a more similar structure to fibrous filters commonly used in air filtration. HFM3 has an asymmetric pore structure and a more fibrous internal network, thus combining two key features of HFM1 and HFM2 for a broader survey of functional characteristics with variable membrane features. Additionally, HFM3 has an apparently higher porosity than the other two membranes (Figure 2G). Notably, PTFE hollow fiber membranes with fibrous pore networks have previously shown success as aerosol filters, albeit with less than ideal efficiency (~90%) for 300 nm particles.³⁶

In addition to pore structure variables, the HFMs in this work were chosen to sample different material properties for a more comprehensive characterization of key parameters for membrane-based air filtration. For example, HFM1 and HFM2 are both constructed of highly hydrophobic materials (polyvinylidene fluoride PVDF and polypropylene PP, respectively), whereas HFM3 has a hydrophilic surface property. Importantly, these differences in surface chemistry may have a meaningful effect on function in aerosol filtration, especially with respect to virus neutralization by immobilizing on the surface, since it has been demonstrated that hydrophobic surfaces can contribute to virus deactivation 46,47 (see also Supporting Information Figure 7). Furthermore, a previous study has shown that hydrophobicity of the membrane can affect the fouling properties of membranes used for aerosol filtration of hygroscopic particles,³⁴ suggesting further study of membrane properties may inform future work designing membranes for aerosol filtration. Importantly, all three materials can tolerate disinfection via 70% ethanol, a common disinfectant available to the general public.

Hollow Fiber Membranes Present Advantageous Pore Features for Aerosol Filtration. The three hollow fiber membranes (HFM) were characterized initially to determine their potential for aerosol filtration (Table 1). In particular, detailed knowledge of the pore structure is advantageous for understanding and predicting the capture of aerosols. Features such as tortuosity (τ) , pore diameter (r_p) , overall porosity (ε) , and membrane thickness (δ) govern flux (J) across the membrane (see eq 3), and therefore knowledge of these parameters can guide the choice of membrane for a particular application.

$$J \propto \frac{\varepsilon \times r_{\rm p}}{\delta \times \tau} \tag{3}$$

Furthermore, tortuosity and pore asymmetry likely affect the capture or separation of particles from air. 48,49 For example, the increased path length associated with higher tortuosity increases diffusion mediated capture for smaller particles. 48 On the other hand, since increased air velocity increases impaction, asymmetric pores with bottlenecks could increase efficiency for larger particles' filtration. Therefore, several techniques were employed to characterize membrane properties.

Scanning electron microscopy (SEM) was used to examine membrane pores in detail (Figure 2, Supporting Information Figures 11–19), revealing variable properties among the three tested membranes. Determination of tortuosity by imaging is not easy; however, examination of several cross-section views by SEM suggests highly branched networks of pores within the membranes. In the case of HFM1, a highly branched, porous network with spongy structure is observed near the lumen, while the shell surface was found to have smaller pores with much lower porosity (Table 1).

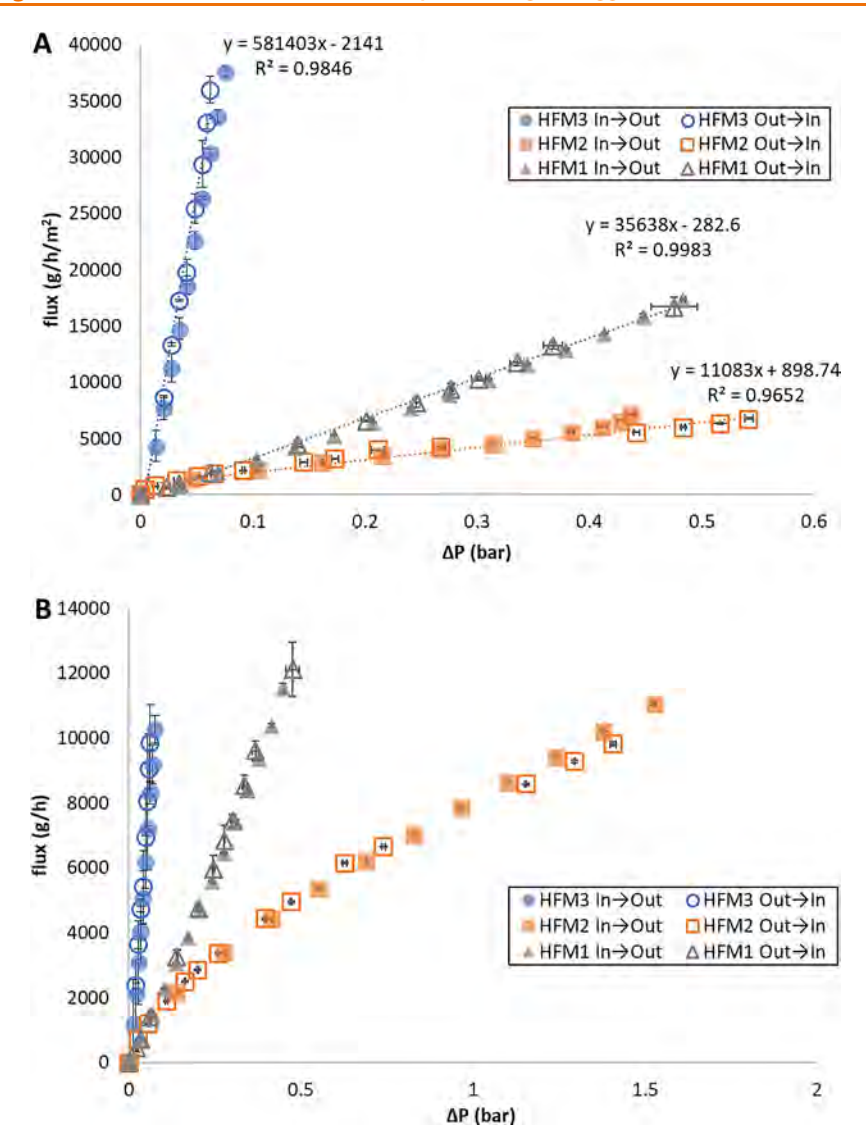


Figure 3. Air permeability characterization of hollow fiber membrane modules. (A) Area-normalized flux for each membrane shows the relationship that larger pore size results in larger permeability, as expected. Filled symbols represent the inside-out (lumen-to-shell flow) mode of operation, and empty symbols represent the outside-in (shell-to-lumen flow) operation. The slope of the trendline is shown for each outside-in mode and indicates the permeability constant for each membrane. ΔP values were adjusted for HFM1 and HFM2 modules as described in the Supporting Information. Plotted values represent the average, and error bars represent the standard deviation (N=3). (B) total throughput for each individual module as a function of transmembrane pressure, not normalized for area to demonstrate actual throughput capacity for each module. ΔP values were *not* adjusted to demonstrate a simplified total capacity per module including flow restrictions from the housing. Plotted values represent the average, and error bars represent the standard deviation (N=3).

The HFM1 fiber was found to have a highly asymmetric pore structure, with significantly wider pore openings in the lumen surface than in the shell surface (~57 nm vs ~1.3 μ m, Supporting Information Figure 11C vs 13C). A similar asymmetric pore structure was also observed in the HFM3 membrane (~140 nm vs ~750 nm, Supporting Information Figure 17C vs 19B), while the HFM2 fibers were notably less variable in pore size at the lumen versus shell surfaces ~40 nm on each side, Supporting Information Figure 14B vs 16C). The result of the imaging analysis suggests that the pore asymmetry of the HFM1 and HFM3 fibers may be make them ideal candidates for more versatile application in air filtration given the potential to tune performance by controlling pore structure (Figure 1).

In addition to SEM, nitrogen porosimetry was also used to characterize the membrane structure for the HFM2 membrane.

The pore size distribution was unobtainable by porosimetry for HFM1 and HFM3 given the limits of nitrogen as the working fluid; however, for HFM2 the result (average ~38 nm pore diameter, Supporting Information Figure 20) was reasonably consistent with SEM analysis (~42–46 nm average pore diameter, Supporting Information Figure 24) and manufacturer specifications. Furthermore, mercury porosimetry data (Supporting Information Figure 21) provided with the generous gift of HFM1 from the START Centre also shows comparable pore distribution to that of SEM analysis (Supporting Information Figure 24).

HFM Modules Demonstrate Predictable Air Transport Properties. As the first step to assessing performance of the three membranes, dead-end mode (all air flow passing through membrane) air permeability was measured for each module (Figure 3). Notably, the flow rate measurements

normalized by area as a function of transmembrane pressure (Figure 3, panel A) demonstrate the expected pattern of permeability values (equivalent to the slope of the linear regression), with the smallest pore size membranes (HFM2, nominal 40 nm pores) showing the lowest permeability and the largest pore size membranes (HFM3, nominal 200 nm pores) showing the highest permeability. This is as expected, given the known relationship between flux and membrane properties (eq 3). While these modules do require a higher pressure as driving force than standard HEPA filters (generally ~0.003 bar⁵⁰), previous work has shown that polymer membranes tend to maintain their initial pressure drop longer than fibrous HEPA filters. 32,51,52 Nonetheless, these results demonstrate that HFM3 coupled to a vacuum pump or compressor operating at ~ 0.5 bar pressure differential would allow filtering the full restaurant air volume every ~7.7 h for a typical small restaurant ($\sim 20 \text{ m} \times \sim 10 \text{ m} \times \sim 2.5 \text{ m}$) (see Supporting Information Detailed Methods for information on calculations). For comparison, a typical HEPA filter (operating at ~ 0.003 bar) could filter the same air volume every ~ 11.9 h.⁵⁰

Zohar et al. derived expressions for the flow of gases through planar microchannels, ⁵³ and adaptation of their solution for cylindrical geometry (see Supporting Information Detailed Methods) results in the following relationship (eq 4)

$$\dot{m}_{\text{singlepore}} = \left(\frac{\pi r^4}{8\delta}\right) \left(\frac{\overline{P}}{RT\mu}\right) (\Delta P)(1 + 8Kn)$$
 (4)

where $\dot{m}_{\rm singlepore}$ is the mass flow rate through a single pore, r is the pore radius, δ is the membrane thickness, \overline{P} is the average absolute pressure in the membrane, R is the gas constant, T is the absolute temperature, μ is the fluid viscosity, and Kn is the Knudsen number defined by the ratio of air mean free path λ and pore diameter $(Kn = \frac{\lambda}{2r})$. Applying this equation for membranes in this study, we find the theoretical predictions agree quite well (Supporting Information Figure 26). Interestingly, the calculations performed assuming circular pore geometry for HFM2 are more accurate than those using planar geometry, despite the elliptical shape of the pores at membrane surfaces, which suggests that circular pore geometry can be assumed for most membranes in this application (Supporting Information Figure 26B). Additionally, comparison of two models for HFM1 demonstrate that consideration of the tight shell surface layer alone is adequate for predicting total flux through the membrane, without the need to consider the more porous/larger pore region of the membrane thickness (Supporting Information Figure 26A). In all cases, the agreement between predicted and measured values provides a basis for predicting functionality of membranes designed for aerosol capture in future work.

Importantly, the direction of air flow (shell-to-lumen vs lumen-to-shell) in each membrane has a minimal effect on the permeability (Figure 3). Given the opportunity to control filtration mechanisms by direction of flow for asymmetric pores (Figure 1), the consistency in permeability regardless of flow direction presents another strong indicator for the value of HFMs as enclosed space aerosol filters. Together, the structural features and transport properties of all three membranes suggest great potential for use as effective aerosol filters even for submicron (submicrometer) particles.

Filtration Testing with a Defined Aerosol Mixture Including a SARS-CoV-2 Mimic Demonstrates Efficient

Particle Removal. Aerosol filtration tests were performed with size-dispersed nanoparticle mixtures (50 nm, 100 nm, 500 nm) including a SARS-CoV-2 mimic (protein coated 100 nm PSL) to determine the aerosol removal efficiency. The SARS-CoV-2 spike protein is a large trimeric assembly that protrudes from the ∼100 nm virus particle and is responsible for binding the ACE2 receptor on human cells to mediate host cell entry; ^{54,55} in this work, a superfolder GFP was immobilized on 100 nm PSL to approximate the presentation of the spike protein on a virus particle surface. As shown in Figure 4, all

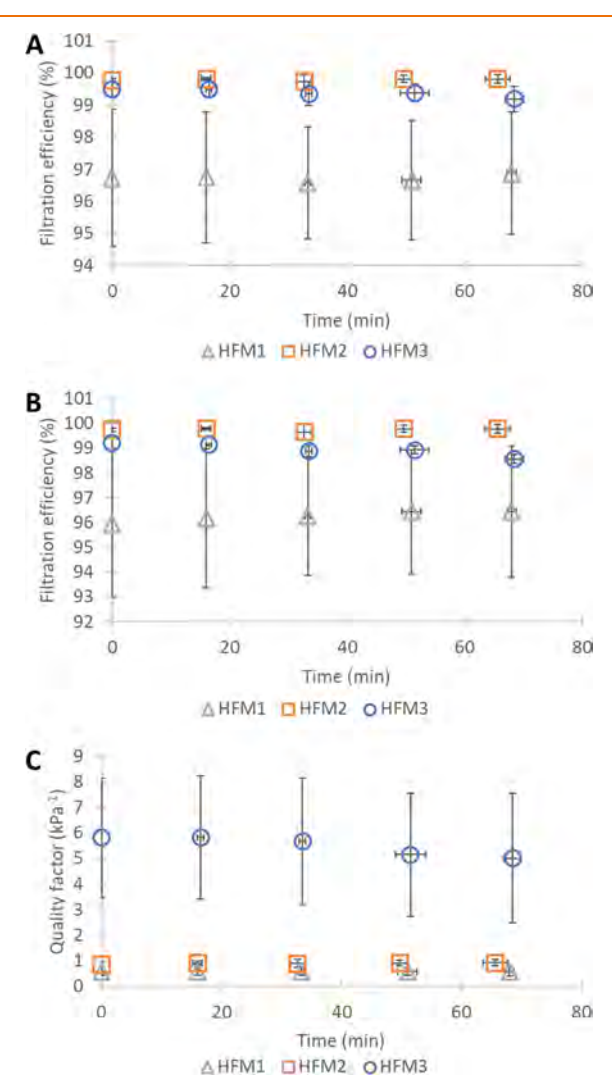


Figure 4. Filtration efficiency of HFMs with controlled size aerosol mixtures (including protein labeled 100 nm synthetic virus mimic) operating in outside-in mode at ~20 SLPM (Standard Liters Per Minute, face velocities (cm/s) of 0.045 ± 0.001 , 0.023 ± 0.004 , and 0.098 ± 0.037 for HFM1, HFM2, and HFM3, respectively). Vertical error bars represent standard deviation of calculated values, and horizontal error bars are the standard deviation of actual measured time from the start of the experiment across the three independent experiments. (A) Filtration efficiency for all particles >300 nm showing excellent filtration for each module. (B) Filtration efficiency for particles in the 300-500 nm size range bin of the optical counter, showing again high efficiency for removing particles in the size range of MPPS (most penetrating particle size) typically used for air filter validation. (C) Quality factor over time for short-term filtration experiments demonstrating no fouling for HFM1 and HFM2 with minimal fouling for HFM3.

three membranes show excellent filtration efficiency in the tested size ranges (particle diameter $0.3-3~\mu m$, the size range most relevant for aerosol virus transmission 5,11,56) over the course of approximately 1 h run time. In particular, the HFM2 fibers with about 40 nm pores showed the expected best performance demonstrating >99.65% rejection for all particles $0.3-3~\mu m$. HFM3 showed the next best average performance, with >98.8% rejection for all particle sizes tested here. The higher fiber packing fractions of HFM2 and HFM3 (Table 1) may also contribute to better aerosol filtration observed in these cases. Of course, all membranes will have some outliers in pore size that are larger than expected, which may explain the few particles that come through for all three membranes even at the particle sizes much larger than the average pore size.

The high filtration efficiency observed for all three membranes in this work suggests the potential for these HFM modules to be applied in air purification for viral aerosols and airborne particle separation applications. Air pollution particulate matter of varying sizes has been shown to have significant impacts on human health. $^{13,15,17,57-59}$ Moreover, it is expected that climate change will continue to increase the levels of air pollution, including potentially $PM_{2.5},^{60,61}$ emphasizing the importance of air cleaning technologies now and in the future. In this application, all three membranes examined here have great potential for removing inhalable particulate matter in a wide range of sizes (<0.1 μm $PM_{0.1},$ <1 μm $PM_{1},$ <2.5 μm $PM_{2.5},$ <10 μm $PM_{10})$ with known detrimental effects on health. $^{57-59}$

Extended Filtration Testing with Ambient Aerosol Shows High Efficiency and Minimal Fouling. In order to demonstrate real-world applicability of HFMs for aerosol capture, filtration with ambient air was performed continuously for approximately 2 days for each HFM. Notably, while the short-term filtration tests cover the most relevant particle sizes for aerosol transmission of viruses, 5,11,56 viral transmission could still occur via smaller aerosols in the range of 100-300 nm. Therefore, in these experiments, the aerosol distribution was measured for all particles >10 nm to further establish filtration efficiency for all aerosol sizes relevant to viral transmission (>100 nm, the size of a single viral particle). As shown in Figure 5, all three HFMs showed consistent performance over 48 h with no significant change in filtration efficiency. Only HFM3 showed a noticeable (but small) reduction in quality factor over the course of 2 days, suggesting that all HFMs (especially HFM1 and HFM2) should have a long effective lifetime as air filters. This observed variation is probably due to the likely differences in the filtration mechanisms for HFM1 and HFM2 compared to HFM3; the shell side pore sizes for HFM1 (~57 nm) and HFM2 (~40 nm) therefore would sieve the vast majority of aerosols, whereas HFM3 has a larger pore size at the shell surface (\sim 140 nm) and allows more aerosols to enter pores and deposit, ultimately reducing the effective pore size over time.

Pseudovirus Aerosols Are Effectively Removed by Hollow Fiber Membrane Air Filtration. Interestingly, few membrane aerosol filtration studies have focused on the properties of the aerosol particles. For example, biologically derived aerosols will often contain complex mixtures of water, surfactants, sugars, proteins, and lipids, which may alter their adhesion to filters or surfaces as compared to rigid particles like polystyrene latex which are often used for aerosol filtration studies. 62,63 Indeed, previous studies have shown the potential

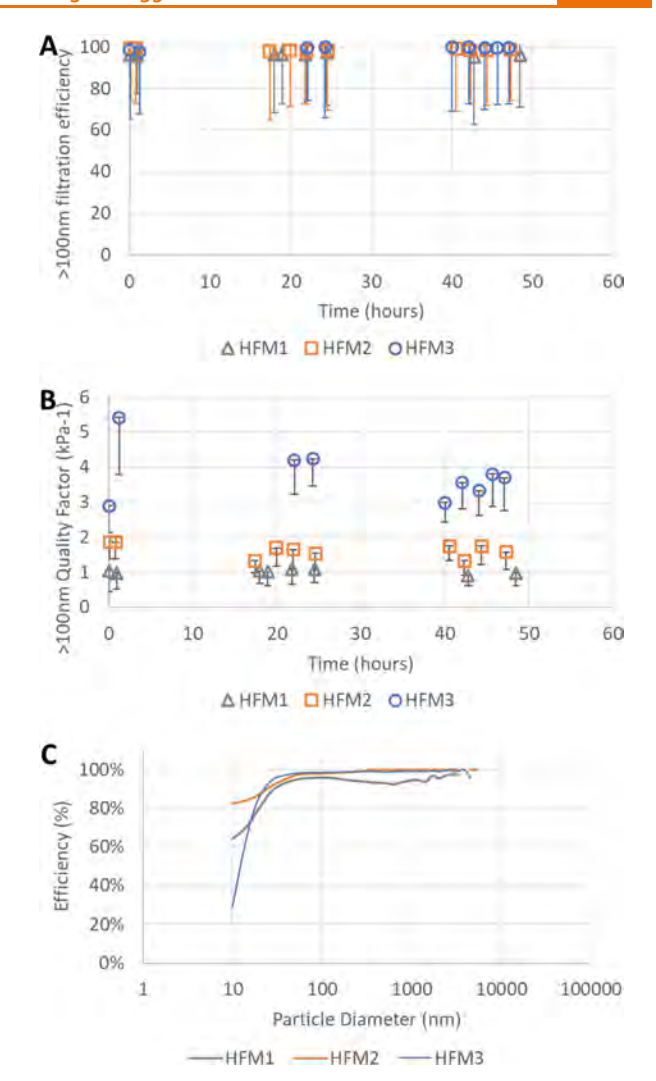


Figure 5. Long-term filtration testing with ambient air in outside-in mode at a constant flow rate of ~20 SLPM. (A) Filtration efficiency for all aerosols >100 nm shows high performance by each HFM over the 48-h test period. Values are calculated from time averaged values over each time window between points with error bars representing the error propagated from the standard deviation of particle counts over the same time windows. (B) Quality factor over 48 h shows no fouling for HFM1 and HFM2, with a small reduction for HFM3 that is driven by a slight increase in pressure drop (see Supporting Information Figure 27). Error bars represent the quality factor value calculated with efficiency minus standard deviation of efficiency from panel A; upper error bars are not included since the efficiency uncertainty results in undefined values of QF when the efficiency is greater than 100% corresponding to upper error bounds in panel A. (C) Filtration efficiency curves for each HFM averaged over the twoday experiment show high efficiency for all particles relevant to viral transmission (>100 nm) for HFM2 and HFM3, consistent with short duration filtration tests.

for accumulation of water on protein- and salt-containing hygroscopic particles. Wang et al. demonstrated that particle hygroscopicity may play a role in pressure drop increases of aerosol membrane filters by leading to water accumulation at the membrane surface that forms films blocking pore openings. Given the importance of particle characteristics, we further confirmed the value of HFMs as enclosed space air filters using a model system consisting of VSV (vesicular stomatitis virus) pseudovirus with a GFP

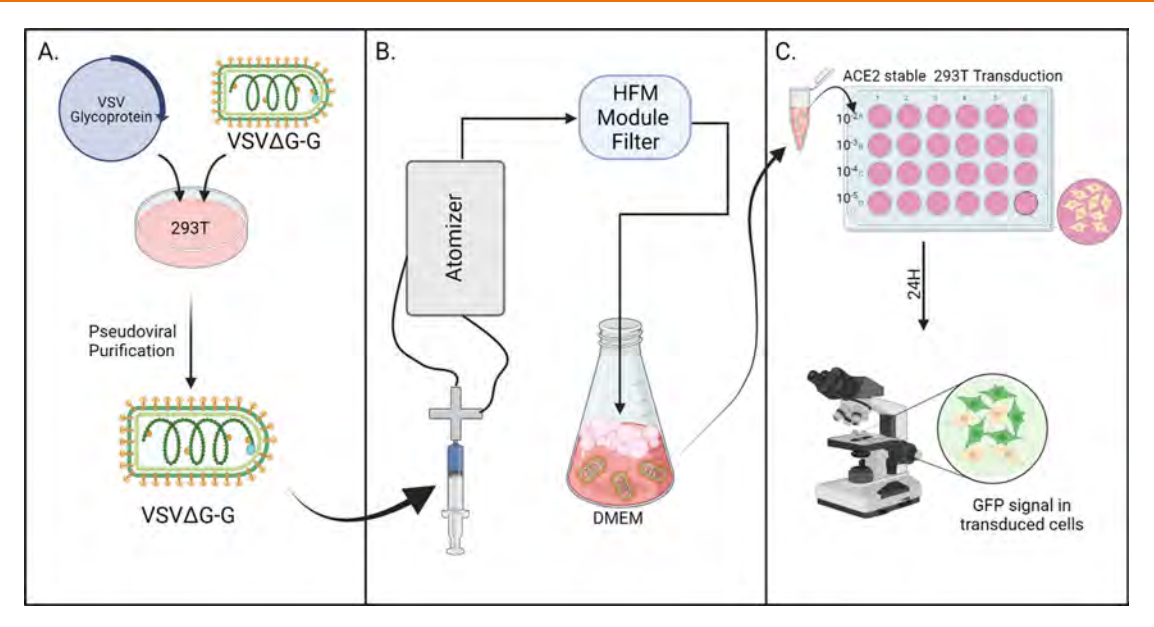


Figure 6. Schematic representation of of pseudovirus production, aerosol filtration studies, and transduction assay. (A) VSV pseudovirus (VSV ΔG +G) was produced in HEK293T cells and purified. (B) VSV ΔG +G was loaded into a syringe pump to the atomizer, and the resulting aerosol was passed through the HFM module filter (or an equivalent length of tubing with no filter) before collection by DMEM solution bubbling. The collected sample was concentrated by centrifugal ultrafiltration (100 kDa MWCO). (D) Pseudoviral transduction assays were performed, wherein serial dilutions of pseudovirus suspensions from aerosol filtration tests are incubated with HEK293T cells that stably express both the LDLR (VSV glycoprotein receptor) and the ACE2 receptor for SARS-CoV-2, resulting in translation of the GFP reporter gene within the VSV ΔG +G genome. Quantification of fluorescent cells by microscopy provide quantitative assessment of active pseudoviral particles. Created with BioRender.com.

ı

reporter gene (Figure 6) for the most accurate picture of filter performance in the desired application. This reporter system is a good approximation of SARS-CoV-2, as both VSV and SARS-CoV-2 are enveloped particles with sizes of approximately ~80-120 nm. 55,65 The particle shape is somewhat different (bullet-shaped VSV versus spherical coronaviruses), but otherwise from an aerosol filtration perspective, recombinant VSV pseudoparticles are an excellent approximation for SARS-CoV-2 virions. Importantly, recombinant VSV pseudotypes have been widely used to study biochemical features of infection and immune responses for a variety of pathogenic viruses in a safer system that is incapable of replicating but transduces GFP expression as a reporter of virus attachment and entry in cell culture models. 66,67 Pseudovirus titer (defined as the number of active transducible pseudovirus particles per milliliter of suspension) is used as a measure of pseudovirus removal/deactivation. In this case, due to the need to sterilize equipment for biosafety concerns, no aerosol counting was performed for direct comparison of the filtration efficiency, as was shown in the case of other filtration tests performed in this work.

As shown in Figure 7, all three HFM modules significantly (p < 0.05) reduced the titer of aerosolized virus as compared to the unfiltered control. Notably, HFM1 with a spongy substructure showed a lower performance (~ 100 -fold reduction, $\sim 99\%$ removal) than HFM2 and HFM3 (both ~ 1000 -fold reduction, $\sim 99.9\%$ removal) in removing active pseudoviral particles from air. Importantly, HFM2 and HFM3 both reduced active pseudoviral levels to below the limit of detection (~ 333 active particles/mL), suggesting that the actual efficiency for these two modules may be higher, but this speculation is tempered by the technical limitations of assays used in this work. It is also worth noting that the aerosol created from pseudovirus suspensions is likely a polydispersed mixture of salt, sugar, and pseudovirus aerosols, since the

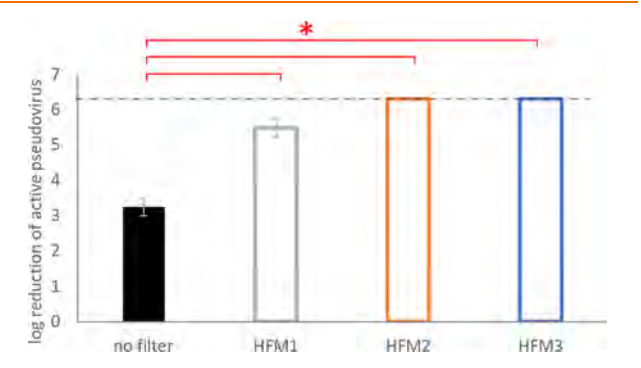


Figure 7. HFM removes pseudovirus aerosol particles effectively as an enclosed space air filter. Pseudovirus titer assay results with VSVΔG +G particles demonstrating high efficiency in removing active pseudovirus. Data are presented as log reduction in active pseudovirus relative to the undiluted transduction control. The 3-log reduction in titer for the unfiltered control shows the losses due to dilution, aerosolization, and recapture of aerosolized pseudovirus in the system (see also Supporting Information Figure 9B). HFM2 and HFM3 performed exceptionally, demonstrating at least 3-log reduction in active pseudovirus compared to the unfiltered control, resulting in titers below the limit of detection for our assay. For HFM1, data represent average of N = 3 independent biological replicates and for HFM2 and HFM3, and data represent the average of the lower limit for log reduction (assay limit of detection). Error bars represent standard deviation for actual log reduction values (HFM1) or assay limit of detection (HFM2 and HFM3). Asterisks indicate statistically significant differences (p < 0.05) comparing the unfiltered control logreduction to each HFM by ANOVA with Tukey HSD posthoc analysis for pairwise comparison. The dashed line represents the average limit of detection for the titering assays. For raw titer data, see Supporting Information Figure 9.

buffer conditions required for pseudovirus stability include various buffer components. Therefore, the filtration behavior with polydisperse ambient aerosols in longer term experiments

may be more representative of efficiency with pseudovirus suspensions. Given the similarity of filtration efficiency for pseudovirus particles, ambient aerosols, and protein-labeled nanoparticles in short-term experiments, it is unlikely that specific composition of the pseudovirus suspension plays a major role in particle removal efficiency.

In this study, the concentration of aerosolized pseudovirus used for HFM testing was relatively high ($\sim 10^5-10^7$ active particles/m³, estimated from collected unfiltered titer and feed titer, respectively), comparable to a closed room with poor circulation where a high virus load emitting infected individual stays for several hours. ⁶⁸ Even in this situation, application of HFMs with >99% filtration efficiency would likely have a significant effect on reducing transmission. Given that most situations outside of hospitals likely have relatively low concentrations of virus in aerosols where even surgical masks with $\sim 30-70\%$ efficiency can reduce transmission rates, ¹¹ the high efficiency separation observed here with HFMs is more than adequate to limit viral spread by aerosols for the majority of real-world situations.

CONCLUSION

This work quantifies the efficacy of microporous hollow fiber membrane modules (with three different structures) as enclosed space air filters for viral aerosol separations using both protein coated PSL particles and active pseudovirus particles. Furthermore, application of commercial microporous HFMs may also find other uses for effective control of indoor air quality given the high efficiency filtration demonstrated here, i.e., as prefilters to lengthen the life span of HEPA air cleaning technologies in highly clean environments like semiconductor manufacturing, especially considering the lack of fouling observed for HFM1 and HFM2 in longer filtration experiments. The higher performances of HFM2 and HFM3 suggest that fibrous internal pore networks may be advantageous as compared to the spongy network of HFM1. These results also lay the foundation for further investigation of HFMs for use in aerosol filtration and, furthermore, provide a framework for design choices in future work developing membrane-based aerosol filtration technologies. For example, our results indicate that reducing the membrane thickness would improve the pressure drop while maintaining high efficiency aerosol separation, since the two thinner membranes (HFM2 and HFM3) had the highest filtration efficiency. Furthermore, long-term filtration experiments also suggest that designing pore structures for sieving separation (i.e., asymmetric pores) may minimize fouling and extend the HFM air filter lifetime while maintaining high efficiency aerosol separation. While the HFMs tested here do not outcompete standard HEPA systems in efficiency or pressure drop, we demonstrate here that commercially available HFMs originally designed for other uses are a highly cost-effective and convenient option for removing viral particles from air for businesses with enclosed spaces (i.e., restaurants, gyms, etc.) to minimize the chances of respiratory illness transmission and mitigate the spread of the COVID-19 pandemic.

ASSOCIATED CONTENT

Supporting Information

The Supporting Information is available free of charge at https://pubs.acs.org/doi/10.1021/acsestengg.1c00369.

Detailed Methods and figures referred to in the text including aerosol filtration system schematics, DLS and Bradford and SDS-PAGE analysis for protein-labeled nanoparticles, schematic for pseudoparticle production method, DLS for aerosol feed mixtures, pseudovirus aerosol experiment optimization, impinger design and photo, raw pseudovirus titer data, schematic overview of this study, photos of disassembled modules, detailed SEM imagining analysis, nitrogen and mercury porosimetry results, contact angle analysis, annotated pore size analysis SEM images, theoretical air flux prediction results, and long-term filtration flow characteristics (PDF)

AUTHOR INFORMATION

Corresponding Author

Dibakar Bhattacharyya — Department of Chemical and Materials Engineering, University of Kentucky, Lexington, Kentucky 40506, United States; orcid.org/0000-0001-9948-9085; Email: db@uky.edu

Authors

Kevin C. Baldridge — Department of Chemical and Materials Engineering, University of Kentucky, Lexington, Kentucky 40506, United States; orcid.org/0000-0003-1829-7714

Kearstin Edmonds — Department of Molecular and Cellular Biochemistry, University of Kentucky, Lexington, Kentucky 40508, United States

Thomas Dziubla — Department of Chemical and Materials Engineering, University of Kentucky, Lexington, Kentucky 40506, United States

J. Zach Hilt – Department of Chemical and Materials Engineering, University of Kentucky, Lexington, Kentucky 40506, United States; oorcid.org/0000-0001-5780-6847

Rebecca E. Dutch – Department of Molecular and Cellular Biochemistry, University of Kentucky, Lexington, Kentucky 40508, United States

Complete contact information is available at: https://pubs.acs.org/10.1021/acsestengg.1c00369

Author Contributions

The manuscript was written through contributions of all authors. All authors have given approval to the final version of the manuscript.

Funding

This research was supported by NIEHS/NIH grant P42ES007380. Partial support was also provided by the NSF-RAPID grant (Award Number: 2030217).

Notes

The content is solely the responsibility of the authors and does not necessarily represent the official views of NIH. The authors declare no competing financial interest.

ACKNOWLEDGMENTS

We gratefully acknowledge the NIEHS superfund research program for funding this research and also for the partial support by the National Science Foundation; Professor Yinan Wei for the gift of purified GFP protein; Dr. Gudipati Chakravarthy, Dr. Sebastian Hernandez, and the START Centre (Dr. Adil Dhalla) in Singapore for the generous supply of tribore hollow fiber modules used in this work and the corresponding mercury porosimetry data; Dr. Nicolas Briot for

training and assistance with SEM; Nick Cprek for assistance with construction of aerosol testing systems; and Rollie Mills, Jacob Concolino, and Dr. Malgorzata Chwatko for their helpful discussions.

REFERENCES

- (1) Li, Y.; Qian, H.; Hang, J.; Chen, X.; Cheng, P.; Ling, H.; Wang, S.; Liang, P.; Li, J.; Xiao, S.; Wei, J.; Liu, L.; Cowling, B. J.; Kang, M. Probable Airborne Transmission of SARS-CoV-2 in a Poorly Ventilated Restaurant. *Build. Environ.* **2021**, *196*, 107788.
- (2) Lu, J.; Gu, J.; Li, K.; Xu, C.; Su, W.; Lai, Z.; Zhou, D.; Yu, C.; Xu, B.; Yang, Z. COVID-19 Outbreak Associated with Air Conditioning in Restaurant, Guangzhou, China, 2020. *Emerg. Infect. Dis. J.* **2020**, 26 (7), 1628.
- (3) Klompas, M.; Baker, M. A.; Rhee, C.; Tucker, R.; Fiumara, K.; Griesbach, D.; Bennett-Rizzo, C.; Salmasian, H.; Wang, R.; Wheeler, N.; Gallagher, G. R.; Lang, A. S.; Fink, T.; Baez, S.; Smole, S.; Madoff, L.; Goralnick, E.; Resnick, A.; Pearson, M.; Britton, K.; Sinclair, J.; Morris, C. A. A SARS-CoV-2 Cluster in an Acute Care Hospital. *Ann. Int. Med.* **2021**, *174* (6), 794–802.
- (4) Chia, P. Y.; Coleman, K. K.; Tan, Y. K.; et al. Detection of Air and Surface Contamination by SARS-CoV-2 in Hospital Rooms of Infected Patients. *Nat. Commun.* **2020**, *11* (1), 2800.
- (5) Liu, Y.; Ning, Z.; Chen, Y.; Guo, M.; Liu, Y.; Gali, N. K.; Sun, L.; Duan, Y.; Cai, J.; Westerdahl, D.; Liu, X.; Xu, K.; Ho, K.; Kan, H.; Fu, Q.; Lan, K. Aerodynamic Analysis of SARS-CoV-2 in Two Wuhan Hospitals. *Nature* **2020**, *582* (7813), 557–560.
- (6) Mousavi, E. S.; Kananizadeh, N.; Martinello, R. A.; Sherman, J. D. COVID-19 Outbreak and Hospital Air Quality: A Systematic Review of Evidence on Air Filtration and Recirculation. *Environ. Sci. Technol.* **2021**, 55 (7), 4134–4147.
- (7) CDC. Delta Variant: What We Know About the Science. https://www.cdc.gov/coronavirus/2019-ncov/variants/delta-variant. html (accessed Sep 16, 2021).
- (8) Bake, B.; Larsson, P.; Ljungkvist, G.; Ljungström, E.; Olin, A. C. Exhaled Particles and Small Airways. *Respir. Res.* **2019**, 20 (1), 8.
- (9) Fennelly, K. P. Particle Sizes of Infectious Aerosols: Implications for Infection Control. *Lancet Respir. Med.* **2020**, *8* (9), 914–924.
- (10) Tran, K.; Cimon, K.; Severn, M.; Pessoa-Silva, C. L.; Conly, J. Aerosol Generating Procedures and Risk of Transmission of Acute Respiratory Infections to Healthcare Workers: A Systematic Review. *PLoS One* **2012**, *7* (4), No. e35797.
- (11) Cheng, Y.; Ma, N.; Witt, C.; Rapp, S.; Wild, P. S.; Andreae, M. O.; Pöschl, U.; Su, H. Face Masks Effectively Limit the Probability of SARS-CoV-2 Transmission. *Science* (80-.). **2021**, 372 (6549), 1439–1443.
- (12) Gonzalez-Rivera, J. C.; Baldridge, K. C.; Wang, D. S.; Patel, K.; Chuvalo-Abraham, J. C. L.; Hildebrandt Ruiz, L.; Contreras, L. M. Post-Transcriptional Air Pollution Oxidation to the Cholesterol Biosynthesis Pathway Promotes Pulmonary Stress Phenotypes. *Commun. Biol.* **2020**, 3 (1), 392.
- (13) Apte, J. S.; Brauer, M.; Cohen, A. J.; Ezzati, M.; Pope, C. A. Ambient PM2.5 Reduces Global and Regional Life Expectancy. *Environ. Sci. Technol. Lett.* **2018**, 5 (9), 546–551.
- (14) West, J. J.; Cohen, A.; Dentener, F.; Brunekreef, B.; Zhu, T.; Armstrong, B.; Bell, M. L.; Brauer, M.; Carmichael, G.; Costa, D. L.; Dockery, D. W.; Kleeman, M.; Krzyzanowski, M.; Künzli, N.; Liousse, C.; Lung, S.-C. C.; Martin, R. V.; Pöschl, U.; Pope, C. A.; Roberts, J. M.; Russell, A. G.; Wiedinmyer, C. What We Breathe Impacts Our Health: Improving Understanding of the Link between Air Pollution and Health. *Environ. Sci. Technol.* **2016**, *50* (10), 4895–4904.
- (15) Turner, M. D.; Henze, D. K.; Hakami, A.; Zhao, S.; Resler, J.; Carmichael, G. R.; Stanier, C. O.; Baek, J.; Sandu, A.; Russell, A. G.; Nenes, A.; Jeong, G.-R.; Capps, S. L.; Percell, P. B.; Pinder, R. W.; Napelenok, S. L.; Bash, J. O.; Chai, T. Differences Between Magnitudes and Health Impacts of BC Emissions Across the United States Using 12 Km Scale Seasonal Source Apportionment. *Environ. Sci. Technol.* 2015, 49 (7), 4362–4371.

- (16) Qu, G.; Li, X.; Hu, L.; Jiang, G. An Imperative Need for Research on the Role of Environmental Factors in Transmission of Novel Coronavirus (COVID-19). *Environ. Sci. Technol.* **2020**, 54 (7), 3730–3732.
- (17) Wu, X.; Nethery, R. C.; Sabath, M. B.; Braun, D.; Dominici, F. Air Pollution and COVID-19 Mortality in the United States: Strengths and Limitations of an Ecological Regression Analysis. *Sci. Adv.* **2020**, *6* (45), No. eabd4049.
- (18) Zhu, Y.; Xie, J.; Huang, F.; Cao, L. Association between Short-Term Exposure to Air Pollution and COVID-19 Infection: Evidence from China. *Sci. Total Environ.* **2020**, 727, 138704.
- (19) Galka, N.; Saxena, A. High Efficiency Air Filtration: The Growing Impact of Membranes. Filtr. Sep. 2009, 46 (4), 22–25.
- (20) Hernández, S.; Lei, S.; Rong, W.; Ormsbee, L.; Bhattacharyya, D. Functionalization of Flat Sheet and Hollow Fiber Microfiltration Membranes for Water Applications. *ACS Sustain. Chem. Eng.* **2016**, *4* (3), 907–918.
- (21) Aher, A.; Thompson, S.; Nickerson, T.; Ormsbee, L.; Bhattacharyya, D. Reduced Graphene Oxide-Metal Nanoparticle Composite Membranes for Environmental Separation and Chloro-Organic Remediation. *RSC Adv.* **2019**, *9* (66), 38547–38557.
- (22) Shen, Y.; Song, W.; Barden, D. R.; Ren, T.; Lang, C.; Feroz, H.; Henderson, C. B.; Saboe, P. O.; Tsai, D.; Yan, H.; Butler, P. J.; Bazan, G. C.; Phillip, W. A.; Hickey, R. J.; Cremer, P. S.; Vashisth, H.; Kumar, M. Achieving High Permeability and Enhanced Selectivity for Angstrom-Scale Separations Using Artificial Water Channel Membranes. *Nat. Commun.* **2018**, *9* (1), 2294.
- (23) Ahmad, I.; Weng, J.; Stromberg, A. J.; Hilt, J. Z.; Dziubla, T. D. Fluorescence Based Detection of Polychlorinated Biphenyls (PCBs) in Water Using Hydrophobic Interactions. *Analyst* **2019**, *144* (2), 677–684.
- (24) van den Hurk, R.; Evoy, S. A Review of Membrane-Based Biosensors for Pathogen Detection. *Sensors* (*Basel*). **2015**, *15* (6), 14045–14078.
- (25) Warsinger, D. M.; Chakraborty, S.; Tow, E. W.; Plumlee, M. H.; Bellona, C.; Loutatidou, S.; Karimi, L.; Mikelonis, A. M.; Achilli, A.; Ghassemi, A.; Padhye, L. P.; Snyder, S. A.; Curcio, S.; Vecitis, C.; Arafat, H. A.; Lienhard, J. H., V A Review of Polymeric Membranes and Processes for Potable Water Reuse. *Prog. Polym. Sci.* **2018**, *81*, 209–237
- (26) Khayet, M. Membranes and Theoretical Modeling of Membrane Distillation: A Review. *Adv. Colloid Interface Sci.* **2011**, 164 (1), 56–88.
- (27) Lu, K.-J.; Zuo, J.; Chung, T.-S. Tri-Bore PVDF Hollow Fibers with a Super-Hydrophobic Coating for Membrane Distillation. *J. Membr. Sci.* **2016**, *514*, 165–175.
- (28) Sardari, K.; Fyfe, P.; Lincicome, D.; Ranil Wickramasinghe, S. Combined Electrocoagulation and Membrane Distillation for Treating High Salinity Produced Waters. *J. Membr. Sci.* **2018**, *564*, 82–96.
- (29) Li, M.; Feng, Y.; Wang, K.; Yong, W. F.; Yu, L.; Chung, T.-S. Novel Hollow Fiber Air Filters for the Removal of Ultrafine Particles in PM2.5 with Repetitive Usage Capability. *Environ. Sci. Technol.* **2017**, *51* (17), 10041–10049.
- (30) Bulejko, P.; Krištof, O.; Dohnal, M.; Svěrák, T. Fine/Ultrafine Particle Air Filtration and Aerosol Loading of Hollow-Fiber Membranes: A Comparison of Mathematical Models for the Most Penetrating Particle Size and Dimensionless Permeability with Experimental Data. *J. Membr. Sci.* **2019**, *592*, 117393.
- (31) Bulejko, P.; Dohnal, M.; Pospíšil, J.; Svěrák, T. Air Filtration Performance of Symmetric Polypropylene Hollow-Fibre Membranes for Nanoparticle Removal. *Sep. Purif. Technol.* **2018**, *197*, 122–128.
- (32) Bulejko, P.; Krištof, O.; Dohnal, M. An Assessment on Average Pressure Drop and Dust-Holding Capacity of Hollow-Fiber Membranes in Air Filtration. *Membranes* **2021**, *11*, 467.
- (33) Wang, L.-Y.; Yu, L. E.; Lai, J.-Y.; Chung, T.-S. Effects of Pluronic F127 on Phase Inversion and Membrane Formation of PAN Hollow Fibers for Air Filtration. *J. Membr. Sci.* **2019**, *584*, 137–147.

- (34) Wang, L.-Y.; Yu, L. E.; Chung, T.-S. Effects of Relative Humidity, Particle Hygroscopicity, and Filter Hydrophilicity on Filtration Performance of Hollow Fiber Air Filters. *J. Membr. Sci.* **2020**, 595, 117561.
- (35) Komaladewi, A.; Aryanti, P.; Surata, I.; Subagia, I. A.; Wenten, I. Surface Modification of Microfiltration Polypropylene Membrane for Molecular Air Filtration. *Int. J. Eng. Emerg. Technol.* **2019**, *4* (1), 74–80.
- (36) Xu, H.; Jin, W.; Wang, F.; Li, C.; Wang, J.; Zhu, H.; Guo, Y. Preparation and Properties of PTFE Hollow Fiber Membranes for the Removal of Ultrafine Particles in PM2.5 with Repetitive Usage Capability. RSC Adv. 2018, 8 (67), 38245–38258.
- (37) Akherati, A.; He, Y.; Coggon, M. M.; Koss, A. R.; Hodshire, A. L.; Sekimoto, K.; Warneke, C.; de Gouw, J.; Yee, L.; Seinfeld, J. H.; Onasch, T. B.; Herndon, S. C.; Knighton, W. B.; Cappa, C. D.; Kleeman, M. J.; Lim, C. Y.; Kroll, J. H.; Pierce, J. R.; Jathar, S. H. Oxygenated Aromatic Compounds Are Important Precursors of Secondary Organic Aerosol in Biomass-Burning Emissions. *Environ. Sci. Technol.* 2020, 54 (14), 8568–8579.
- (38) Leung, W. W.-F.; Sun, Q. Charged PVDF Multilayer Nanofiber Filter in Filtering Simulated Airborne Novel Coronavirus (COVID-19) Using Ambient Nano-Aerosols. Sep. Purif. Technol. 2020, 245, 116887.
- (39) Leung, W. W. F.; Sun, Q. Electrostatic Charged Nanofiber Filter for Filtering Airborne Novel Coronavirus (COVID-19) and Nano-Aerosols. Sep. Purif. Technol. 2020, 250, 116886.
- (40) Malloy, J.; Quintana, A.; Jensen, C. J.; Liu, K. Efficient and Robust Metallic Nanowire Foams for Deep Submicrometer Particulate Filtration. *Nano Lett.* **2021**, *21* (7), 2968–2974.
- (41) Palika, A.; Armanious, A.; Rahimi, A.; Medaglia, C.; Gasbarri, M.; Handschin, S.; Rossi, A.; Pohl, M. O.; Busnadiego, I.; Gübeli, C.; Anjanappa, R. B.; Bolisetty, S.; Peydayesh, M.; Stertz, S.; Hale, B. G.; Tapparel, C.; Stellacci, F.; Mezzenga, R. An Antiviral Trap Made of Protein Nanofibrils and Iron Oxyhydroxide Nanoparticles. *Nat. Nanotechnol.* **2021**, *16* (8), 918–925.
- (42) Bonfim, D. P. F.; Cruz, F. G. S.; Bretas, R. E. S.; Guerra, V. G.; Aguiar, M. L. A Sustainable Recycling Alternative: Electrospun PET-Membranes for Air Nanofiltration. *Polymers* **2021**, *13*, 1166.
- (43) Yu, L.; Peel, G. K.; Cheema, F. H.; Lawrence, W. S.; Bukreyeva, N.; Jinks, C. W.; Peel, J. E.; Peterson, J. W.; Paessler, S.; Hourani, M.; Ren, Z. Catching and Killing of Airborne SARS-CoV-2 to Control Spread of COVID-19 by a Heated Air Disinfection System. *Mater. Today Phys.* **2020**, *15*, 100249.
- (44) Qiao, Y.; Yang, M.; Marabella, I. A.; McGee, D. A. J.; Aboubakr, H.; Goyal, S.; Hogan Jr, C. J.; Olson, B. A.; Torremorell, M. Greater than 3-Log Reduction in Viable Coronavirus Aerosol Concentration in Ducted Ultraviolet-C (UV–C) Systems. *Environ. Sci. Technol.* **2021**, *55* (7), 4174–4182.
- (45) RStudio Team. RStudio: Integrated Development Environment for R, Boston, MA, 2021.
- (46) Xue, X.; Ball, J. K.; Alexander, C.; Alexander, M. R. All Surfaces Are Not Equal in Contact Transmission of SARS-CoV-2. *Matter* **2020**, 3 (5), 1433–1441.
- (47) Kalbfuss, B.; Wolff, M.; Geisler, L.; Tappe, A.; Wickramasinghe, R.; Thom, V.; Reichl, U. Direct Capture of Influenza A Virus from Cell Culture Supernatant with Sartobind Anion-Exchange Membrane Adsorbers. *J. Membr. Sci.* **2007**, 299 (1), 251–260.
- (48) Griffiths, I. M.; Mitevski, I.; Vujkovac, I.; Illingworth, M. R.; Stewart, P. S. The Role of Tortuosity in Filtration Efficiency: A General Network Model for Filtration. *J. Membr. Sci.* **2020**, 598, 117664
- (49) Wang, L.-Y.; Yong, W. F.; Yu, L. E.; Chung, T.-S. Design of High Efficiency PVDF-PEG Hollow Fibers for Air Filtration of Ultrafine Particles. *J. Membr. Sci.* 2017, 535, 342–349.
- (50) U.S. Department of Energy. Specification for HEPA Filters Used by DOE Contractors; Washington, DC, 2015.
- (51) Bulejko, P.; Svěrák, T.; Dohnal, M.; Pospíšil, J. Aerosol Filtration Using Hollow-Fiber Membranes: Effect of Permeate

- Velocity and Dust Amount on Separation of Submicron TiO2 Particles. *Powder Technol.* **2018**, *340*, 344–353.
- (52) Novick, V. J.; Monson, P. R.; Ellison, P. E. The Effect of Solid Particle Mass Loading on the Pressure Drop of HEPA Filters. *J. Aerosol Sci.* **1992**, 23 (6), 657–665.
- (53) ZOHAR, Y.; LEE, S. Y. U. K. K.; LEE, W. Y. I. N.; JIANG, L.; TONG, P. I. N. Subsonic Gas Flow in a Straight and Uniform Microchannel. *J. Fluid Mech.* **2002**, *472*, 125–151.
- (54) Hoffmann, M.; Kleine-Weber, H.; Schroeder, S.; Krüger, N.; Herrler, T.; Erichsen, S.; Schiergens, T. S.; Herrler, G.; Wu, N.-H.; Nitsche, A.; et al. SARS-CoV-2 Cell Entry Depends on ACE2 and TMPRSS2 and Is Blocked by a Clinically Proven Protease Inhibitor. *Cell* **2020**, *181* (2), 271–280 others.
- (55) Ke, Z.; Oton, J.; Qu, K.; Cortese, M.; Zila, V.; McKeane, L.; Nakane, T.; Zivanov, J.; Neufeldt, C. J.; Cerikan, B.; Lu, J. M.; Peukes, J.; Xiong, X.; Kräusslich, H.-G.; Scheres, S. H. W.; Bartenschlager, R.; Briggs, J. A. G. Structures and Distributions of SARS-CoV-2 Spike Proteins on Intact Virions. *Nature* **2020**, 588 (7838), 498–502.
- (56) Lee, B. U. Minimum Sizes of Respiratory Particles Carrying SARS-CoV-2 and the Possibility of Aerosol Generation. *Int. J. Environ. Res. Public Health* **2020**, *17* (19), 6960.
- (57) Polichetti, G.; Cocco, S.; Spinali, A.; Trimarco, V.; Nunziata, A. Effects of Particulate Matter (PM10, PM2.5 and PM1) on the Cardiovascular System. *Toxicology* **2009**, *261* (1), 1–8.
- (58) Kappos, A. D.; Bruckmann, P.; Eikmann, T.; Englert, N.; Heinrich, U.; Höppe, P.; Koch, E.; Krause, G. H. M.; Kreyling, W. G.; Rauchfuss, K.; Rombout, P.; Schulz-Klemp, V.; Thiel, W. R.; Wichmann, H.-E. Health Effects of Particles in Ambient Air. *Int. J. Hyg. Environ. Health* **2004**, 207 (4), 399–407.
- (\$9) Schraufnagel, D. E. The Health Effects of Ultrafine Particles. *Exp. Mol. Med.* **2020**, 52 (3), 311–317.
- (60) Jacob, D. J.; Winner, D. A. Effect of Climate Change on Air Quality. *Atmos. Environ.* **2009**, 43 (1), 51–63.
- (61) Kinney, P. L. Climate Change, Air Quality, and Human Health. *Am. J. Prev. Med.* **2008**, *35* (5), 459–467.
- (62) Kim, Y.; Wellum, G.; Mello, K.; Strawhecker, K. E.; Thoms, R.; Giaya, A.; Wyslouzil, B. E. Effects of Relative Humidity and Particle and Surface Properties on Particle Resuspension Rates. *Aerosol Sci. Technol.* **2016**, *50* (4), 339–352.
- (63) Ono, K.; Mizushima, Y.; Furuya, M.; Kunihisa, R.; Tsuchiya, N.; Fukuma, T.; Iwata, A.; Matsuki, A. Direct Measurement of Adhesion Force of Individual Aerosol Particles by Atomic Force Microscopy. *Atmosphere* **2020**, *11*, 489.
- (64) Mikhailov, E.; Vlasenko, S.; Niessner, R.; Pöschl, U. Interaction of Aerosol Particles Composed of Protein and Saltswith Water Vapor: Hygroscopic Growth and Microstructural Rearrangement. *Atmos. Chem. Phys.* **2004**, *4* (2), 323–350.
- (65) Thomas, D.; Newcomb, W. W.; Brown, J. C.; Wall, J. S.; Hainfeld, J. F.; Trus, B. L.; Steven, A. C. Mass and Molecular Composition of Vesicular Stomatitis Virus: A Scanning Transmission Electron Microscopy Analysis. *J. Virol.* 1985, 54 (2), 598–607.
- (66) Li, Q.; Liu, Q.; Huang, W.; Li, X.; Wang, Y. Current Status on the Development of Pseudoviruses for Enveloped Viruses. *Rev. Med. Virol.* **2018**, 28 (1), e1963.
- (67) Condor Capcha, J. M.; Lambert, G.; Dykxhoorn, D. M.; Salerno, A. G.; Hare, J. M.; Whitt, M. A.; Pahwa, S.; Jayaweera, D. T.; Shehadeh, L. A. Generation of SARS-CoV-2 Spike Pseudotyped Virus for Viral Entry and Neutralization Assays: A 1-Week Protocol. Frontiers in Cardiovascular Medicine 2021, 7, 381.
- (68) Riediker, M.; Tsai, D.-H. Estimation of Viral Aerosol Emissions From Simulated Individuals With Asymptomatic to Moderate Coronavirus Disease 2019. *JAMA Netw. Open* **2020**, 3 (7), No. e2013807.

Supporting Information

Demonstration of Hollow Fiber Membrane-Based Enclosed Space Air Remediation for Capture of an Aerosolized Synthetic SARS-CoV-2 Mimic and Pseudovirus Particles

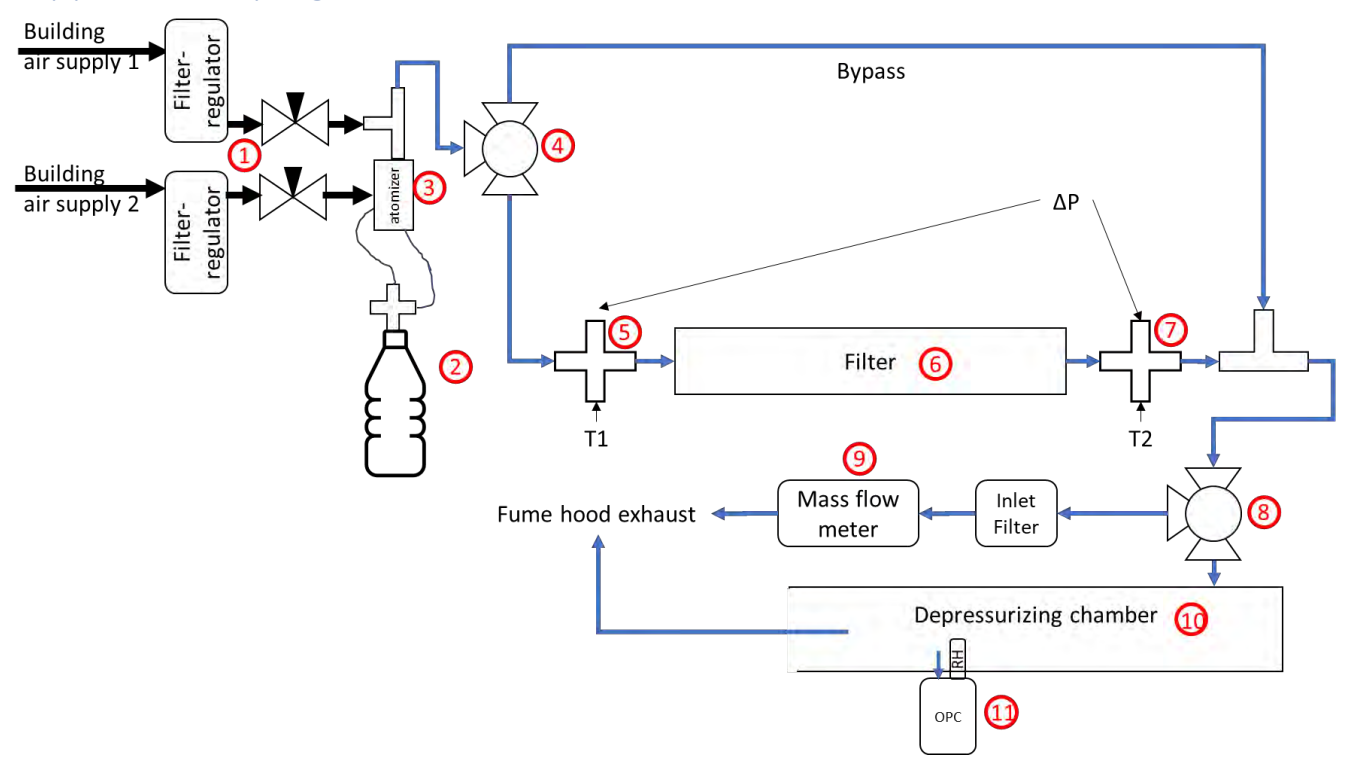
Kevin C. Baldridge^a, Kearstin Edmonds^b, Thomas Dziubla^a, J. Zach Hilt^a, Rebecca E. Dutch^b, Dibakar Bhattacharyya^a*

^a University of Kentucky, Department of Chemical and Materials Engineering, Lexington KY, 40506, United States

^b University of Kentucky, Department of Molecular and Cellular Biochemistry, Lexington KY, 40508, United States

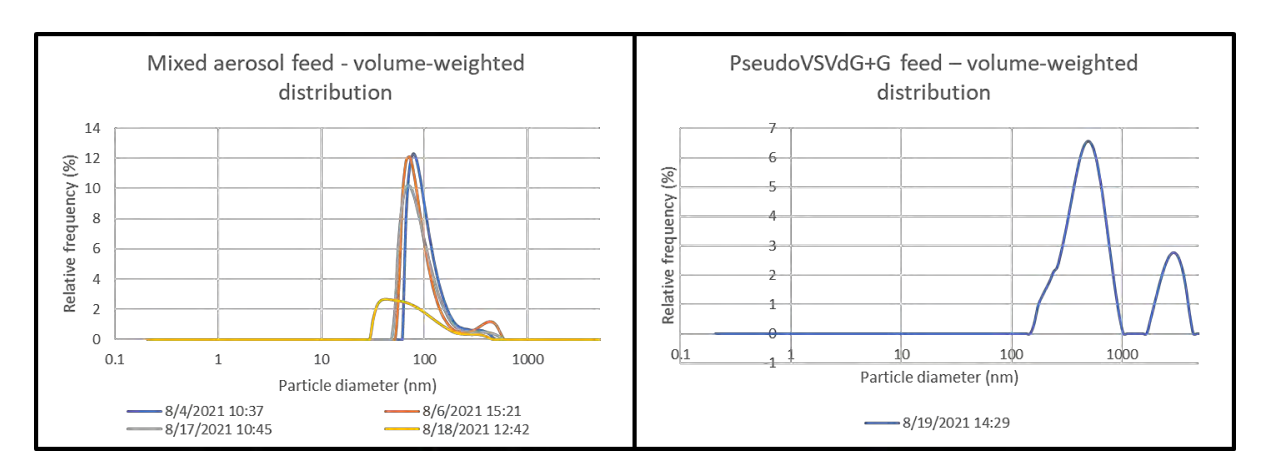
*Email: DB@uky.edu

Supplementary Figures

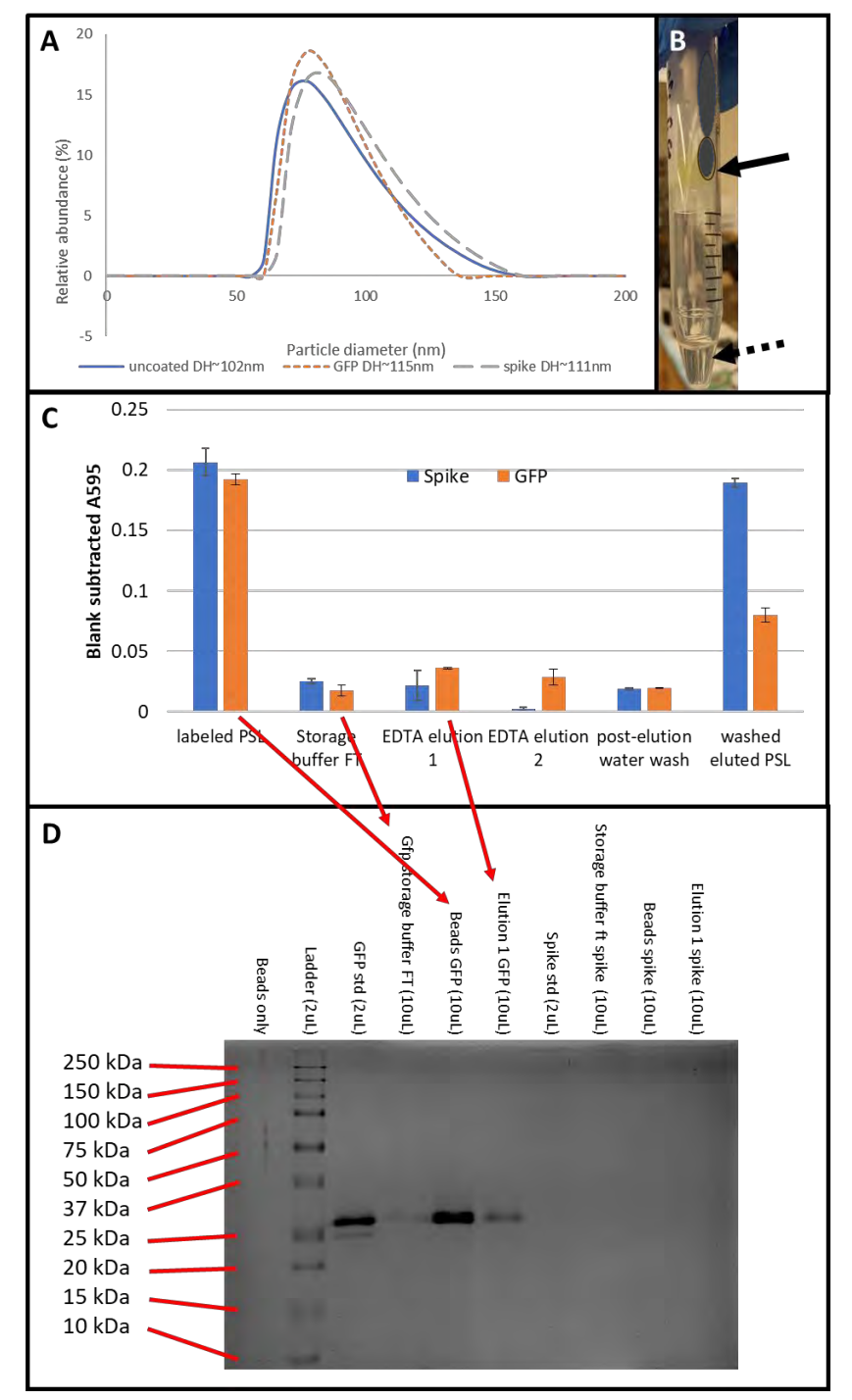


Supplementary figure 1. Schematic of filtration testing apparatus

Building air is generated with a dehumidifier and MERV13 intake filter, and supplied for this work through filtered regulators (1) (Speedaire). The atomizer feed bottle was adapted from an 8oz polymer bottle with fitting mounted in lid (2), and the aerosol was generated by a collision atomizer (3) (TSI 3076). Ball valves (4 and 8) control the flow of air through bypass or HFM (6) for paired unfiltered sampling. Thermocouples (UEi test instruments, model DT304) and differential pressure gauge (Sper Scientific, manometer 840083) were attached as shown at (5) and (7). A mass flow meter (9) (TSI, model 4043) was connected to one outlet. A depressurizing chamber (10) was constructed of a rolled and taped sheet of PTFE, with ports cut for insertion of the RH/Temp probe and isokinetic intake for the optical particle counter (11) (MetOne GT-526S). All tubing was PTFE ½" OD tubing except for the connections to the mass flow meter and tubings from building to atomizer, which are nylon ½" OD.



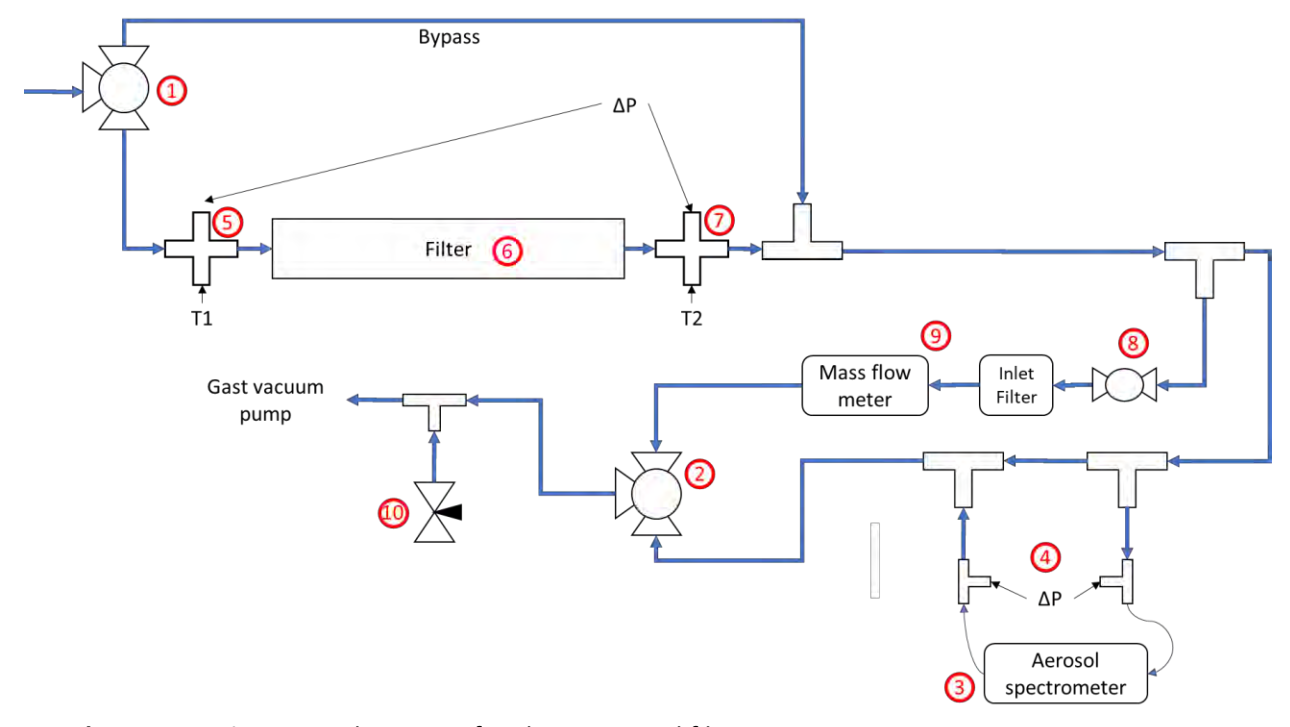
Supplementary Figure 2. DLS characterization of mixed nanoparticle aerosol feed (50nm gold, 100nm polystyrene+spike protein/GFP, 500nm polystyrene) and pseudovirus aerosol feed



Supplementary Figure 3.
Characterization of protein-labeling on 100nm PSL-COOH by dynamic light scattering

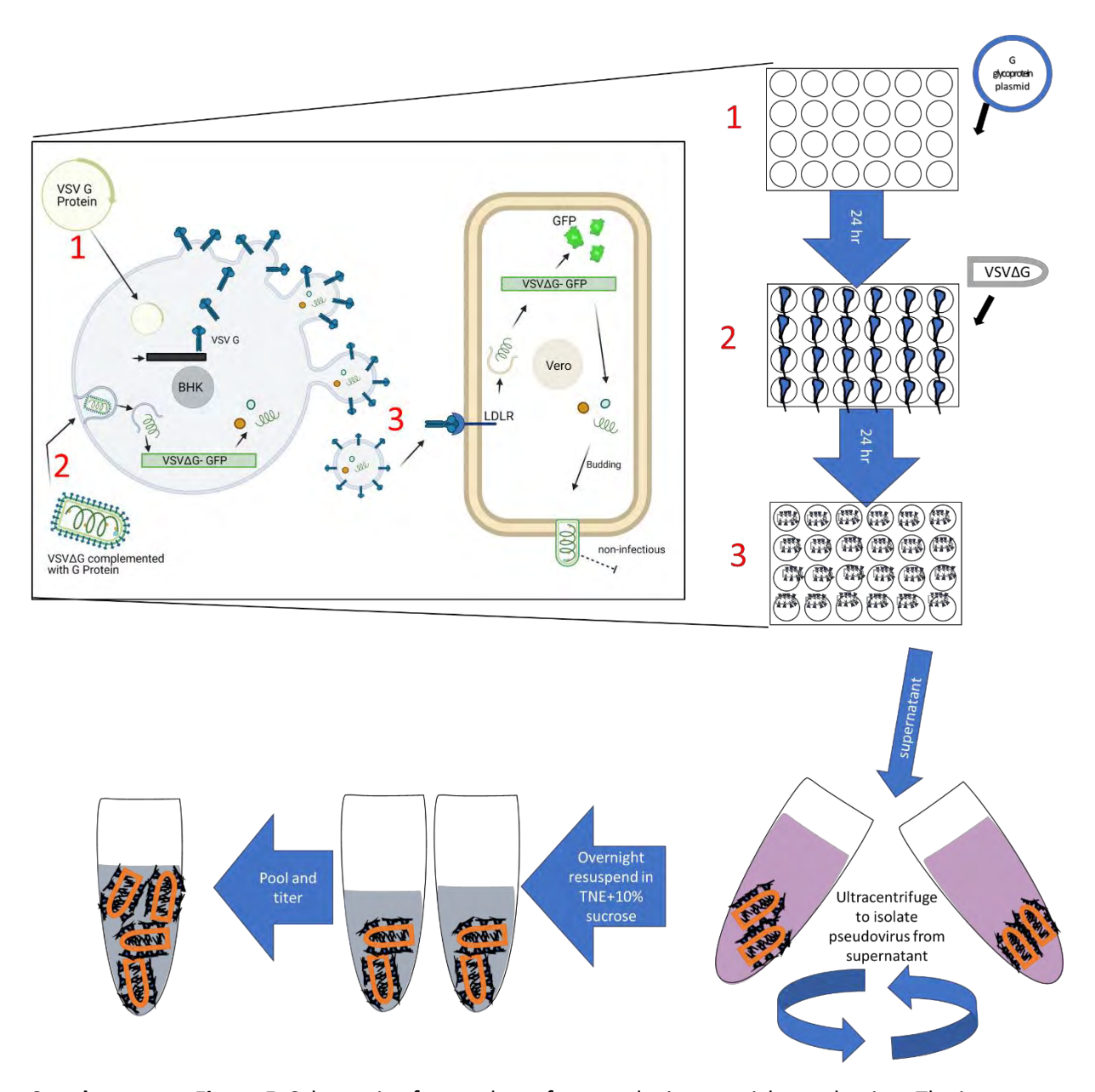
A) Dynamic Light Scattering measurements were performed as a secondary measure of protein labeling, demonstrating the increase in hydrodynamic diameter (and the volumeweighted size distribution) associated with successful immobilization of protein on the surface of PSL NPs for both spike and GFP. B) After several weeks of storage, GFP-labeled 100nm PSL-COOH were concentrated by ultrafiltration through 100kDa MWCO centrifuge filter to verify stable labeling. Solid arrow shows the clearly green nanoparticles, and the dotted line arrow shows the clear permeate with no obvious GFP. C) Bradford assays were used to quantify protein in the storage and elution of protein-labeled PSL after approximately three months of storage at 4C, demonstrating clear stability in storage buffer and subsequent elution of immobilized protein for the case of GFP. For Spike protein, the differences were less pronounced but still suggest successful protein labeling

(reduced signal for PSL after elution) albeit with less stability (given the storage FT is similar signal to the eluted protein). **D**) After approximately three months of storage, GFP-labeled beads were analyzed using a 100 kDa MWCO centrifuge filter to show stability of labeling, with the storage buffer flow-through (lane 4) showing that minimal protein released from beads over three months of storage and the subsequent EDTA elution 1 (lane 6) showing release of immobilized protein when EDTA was included to disrupt nickel/his-tag interactions. Spike protein (including pure protein control) was determined to be degraded after approximately 3 months given the lack of bands or Bradford signal when analyzed by the same process as the GFP-labeled beads.

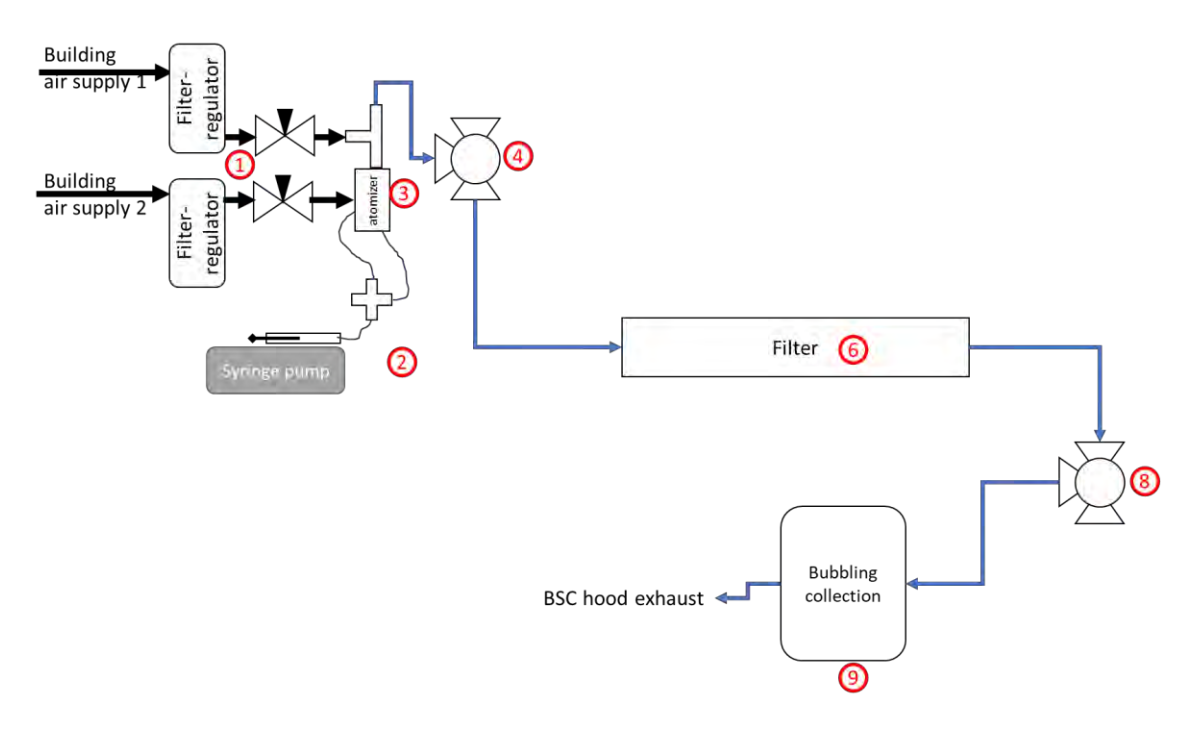


Supplementary Figure 4. Schematic of ambient aerosol filtration testing apparatus

Ambient air is drawn in through ½" PTFE tubing connected to a ball valve (1) for switching between HFM filter (6) and bypass. Thermocouples (UEi test instruments, model DT304) and differential pressure gauge (Sper Scientific 840083 or VWR 33500-086) were attached as shown at (5) and (7). Branches inline along with a downstream ball valve (2) allow switching between the miniWRAS 1371 (3) and the mass flow meter (9). Branches with differential pressure gauge (Sper Scientific 840083 or VWR 33500-086) immediately adjacent at (4) to the miniWRAS were included to monitor pressure differential to protect the miniWRAS pump. The ball valve at (8) was included to prevent backflow when the ball valve at (2) was directed to the miniWRAS, and the needle valve at (10) was included as a relief valve to modulate pressure drop across the filter during experiments measured at (5) and (7). All tubing upstream of the miniWRAS was ½" OD PTFE to match other filtration experiments in this work, except for the short connections between branches at (4) which were ½" nylon, and connections from (4) to miniWRAS were the included tubing (1/4" tygon inlet and 1/8" nylon outlet) with the isokinetic sampler accessory for the miniWRAS. Downstream of the miniWRAS and the inlet tubing for the mass flow meter were ½" nylon.

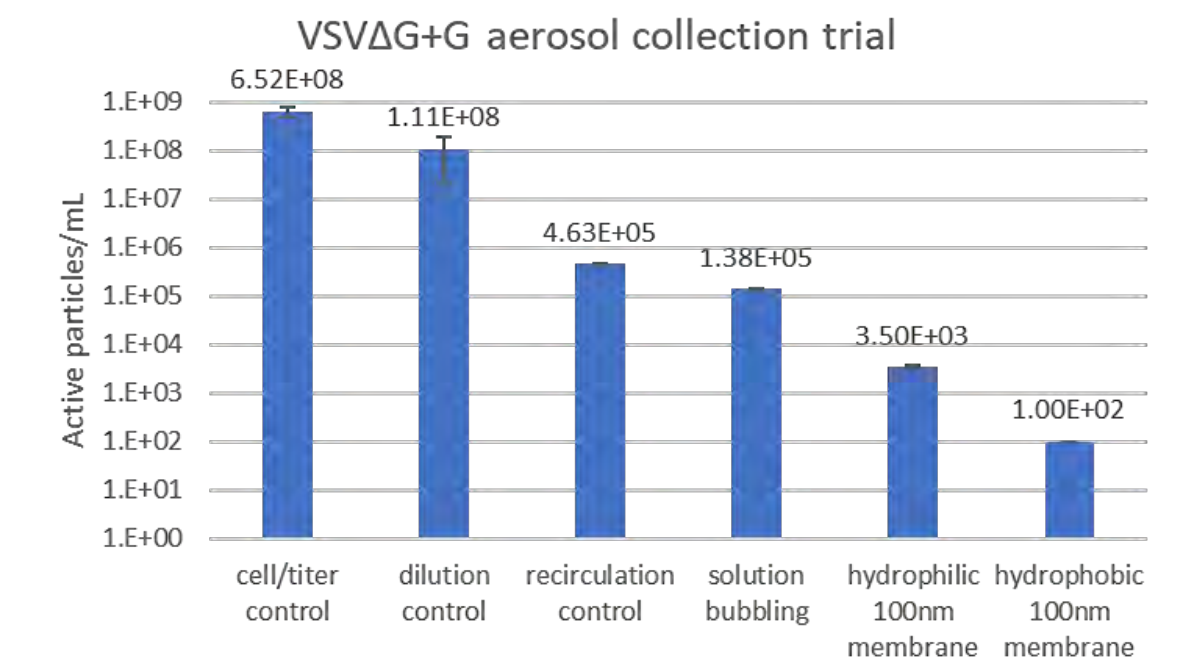


Supplementary Figure 5. Schematic of procedures for pseudovirus particle production. The inset highlights the process occurring at the cell level, within the plates shown for the schematic purification scheme at right. BHK cells are baby hamster kidney cells. $VSV\Delta G$ is the vesicular stomatitis virus (VSV) recombinant pseudovirus lacking the VSV G glycoprotein, and LDLR is the low-density-lipoprotein receptor (mammalian target of G protein). GFP is green fluorescent protein. TNE is 1x TNE buffer (50mM Tris-HCL, 150mM NaCl, and 1mM EDTA). Figure created using Biorender.com



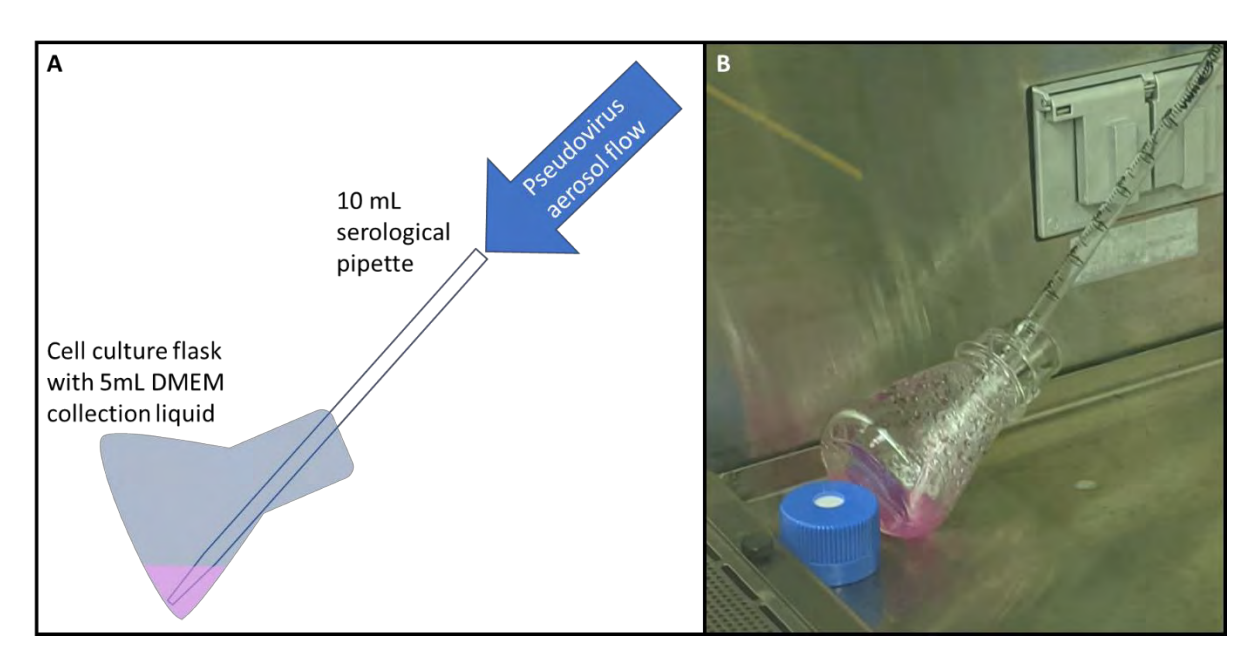
Supplementary figure 6. Schematic of filtration testing apparatus for pseudoviral aerosol tests

The system was adapted to a biological safety cabinet (BSC) and modified as shown for pseudovirus aerosol filtration tests, with substitution of the reservoir bottle by a syringe pump (2) for more controlled dosing and reduced working volume. Additionally, the mass flow meter, temperature probes, pressure probes, and particle counter were all removed to prevent contamination with biohazardous pseudovirus. The bypass was removed, and the HFM (6) was instead swapped out for an equal length of tubing as the unfiltered control. Finally, bubbling collection (9) was performed in 5mL of DMEM mediain a 125mL or 250mL bubbling flask, and a 10mL serological pipette without the plug filter was used to focus the air stream into the DMEM media (see Supplementary Figure 7)A section of ¼" O.D. tygon tubing was used to connect the impinger (9) to the ball valve downstream (8) of HFM module, and ¼" OD nylon tubing connected each needle valve to the atomizer; all other tubing was ½" OD Teflon.

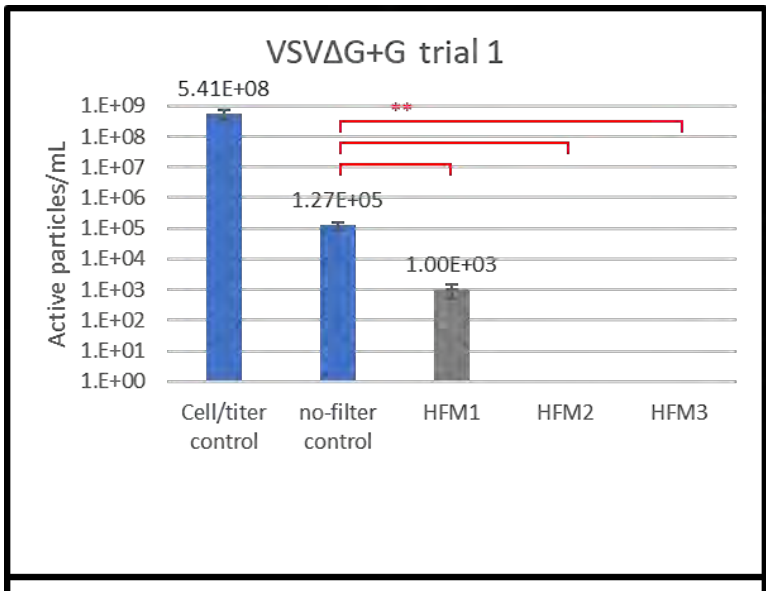


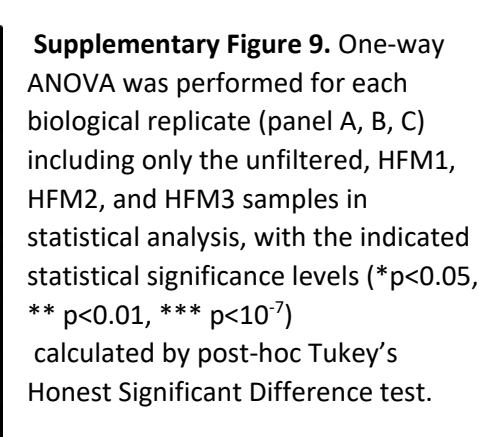
Supplementary Figure 7. Optimization of aerosolized pseudovirus collection method.

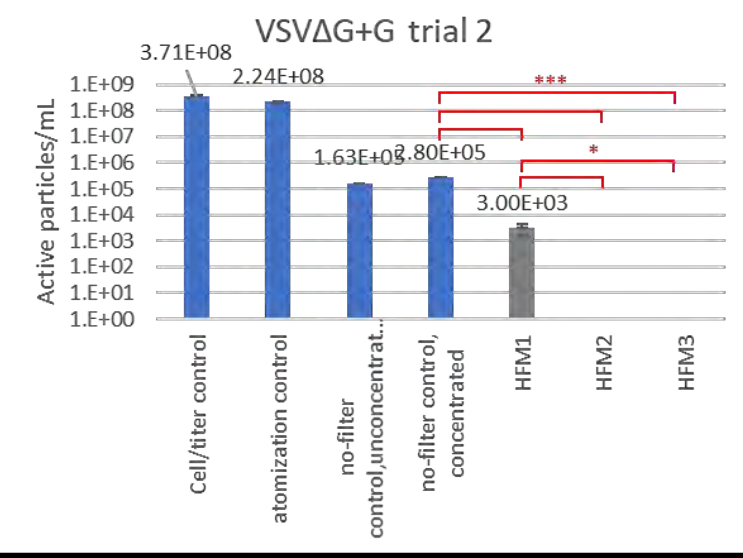
As an initial test, VSV Δ G+G pseudovirus particles were atomized and collected by three different methods to determine the most effective procedure for later filtration experiments with VSV Δ G+SGP pseudovirus particles. Significant losses are notable even with the dilution control, and almost 10k-fold reduction in active titer was observed for the best case scenario of collection by bubbling through DMEM+FBS media. Flat sheet membranes (100nm pores) with hydrophilic (Durapore VVPP) or hydrophobic (Durapore PVDF) character were both tested for collection and resulted in lower active titer than collection by solution bubbling. Note that the hydrophobic membrane titer is essentially at the limit of detection for this assay and therefore is questionable in terms of the numerical value. Error bars represent standard deviation (N=2) of the titer assay technical duplicates.

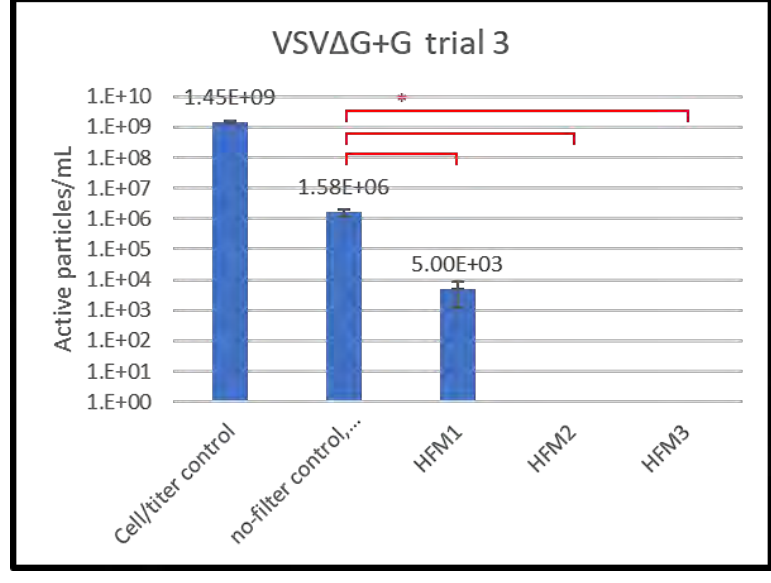


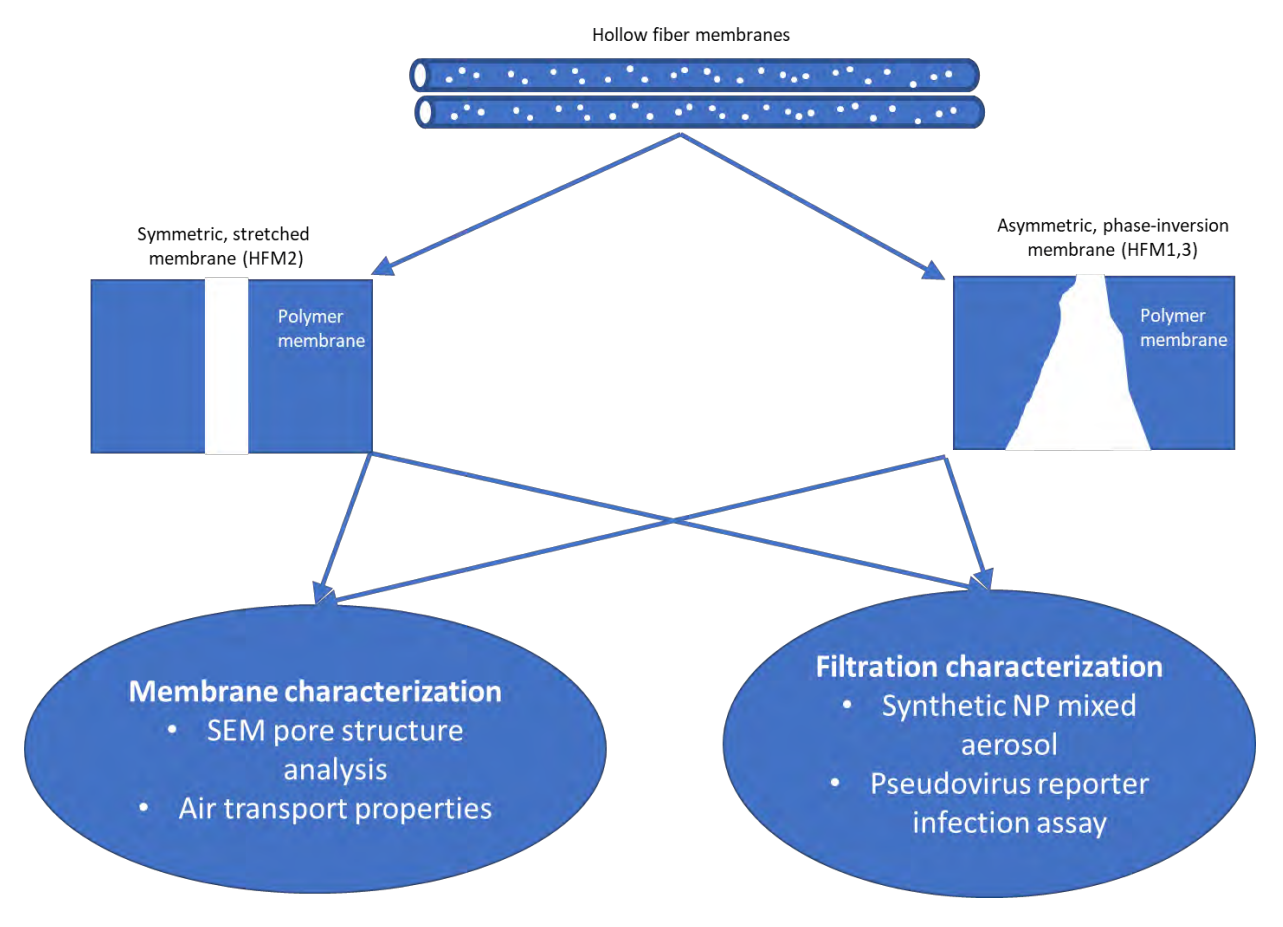
Supplementary Figure 8. Impinger design (A) and photo (B) of actual example. The design consists of a 10 mL serological pipette (with the cotton plugged end broken off) taped to the end of ¼" OD outlet tubing downstream of the HFM module which served to focus the airstream containing pseudovirus aerosols into the collection liquid. The 5mL DMEM collection liquid was contained in a cell culture flask (125mL or 250mL) for the duration of collection, then the cap of cell culture flask was closed during remaining filtration experiments before collection into membrane concentrator cassettes (see Supplementary detailed methods for more information).



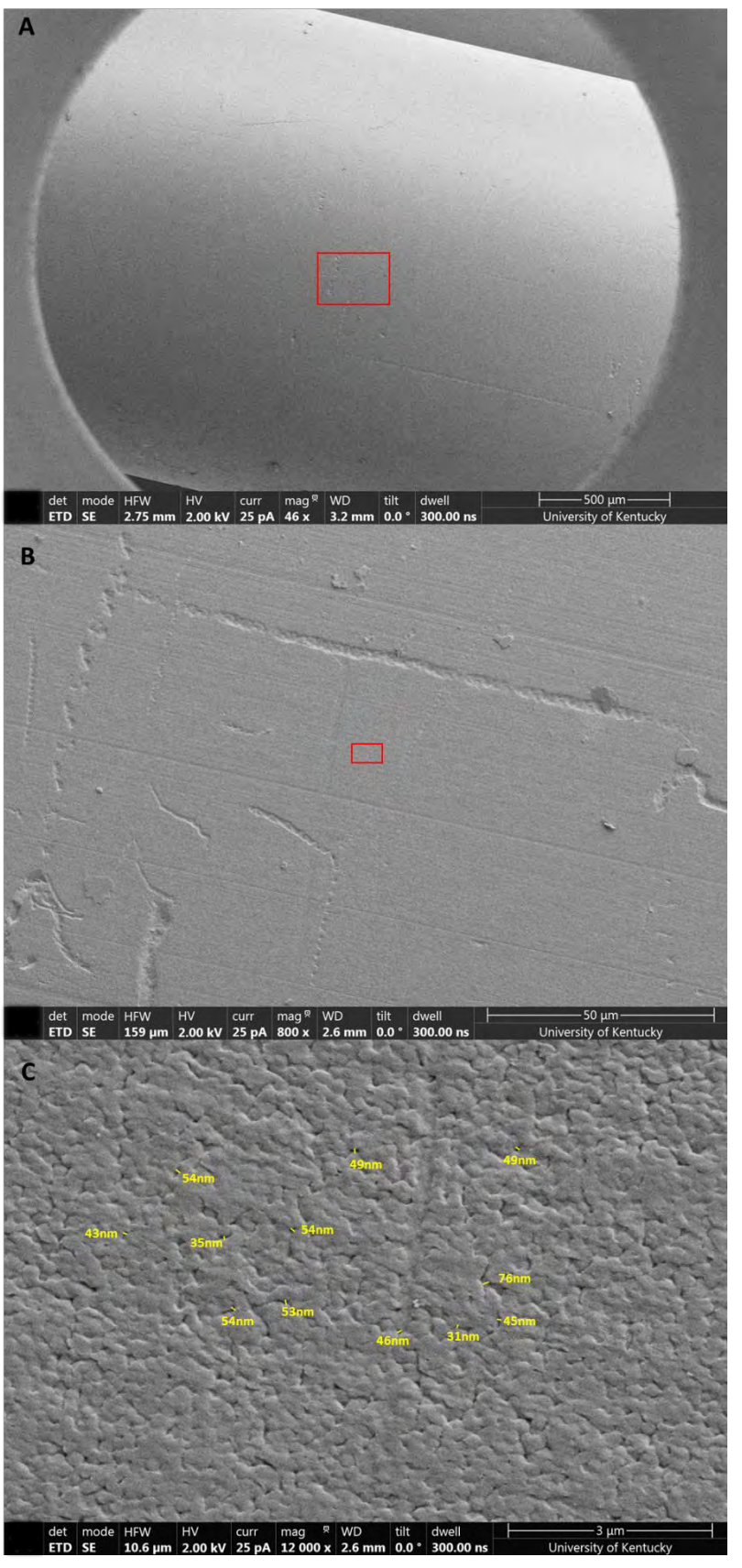






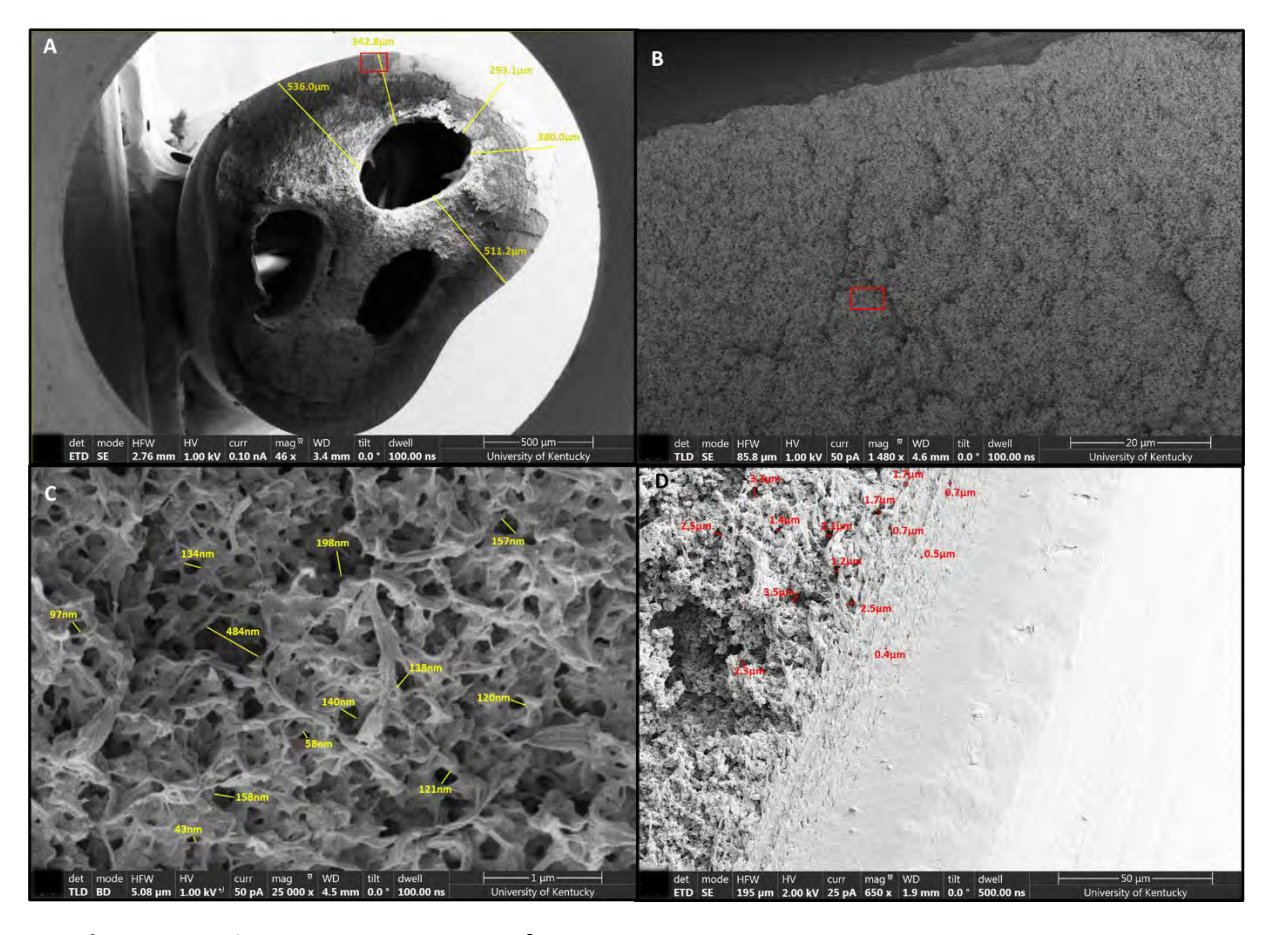


Supplementary Figure 10. Overview of membrane air filtration studies



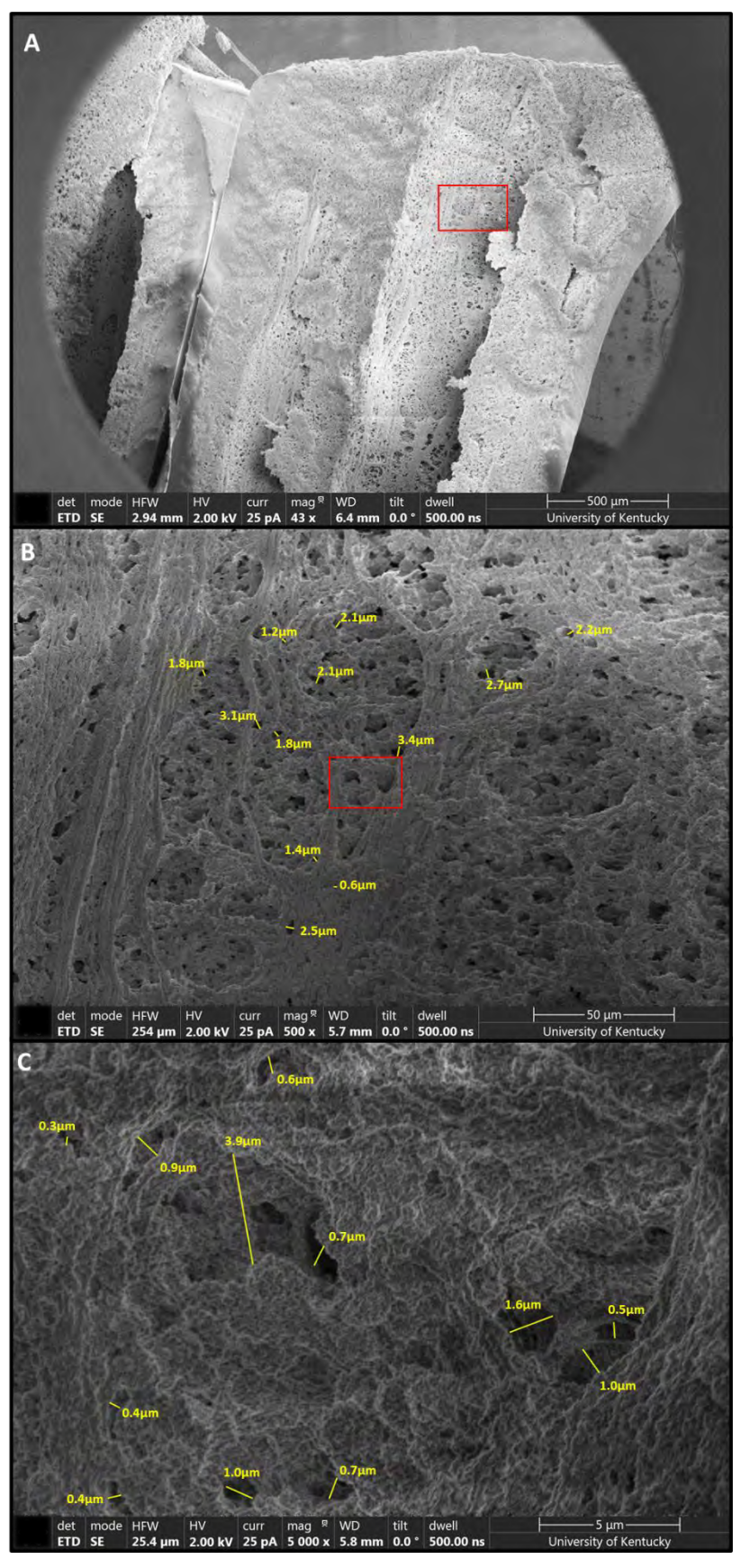
Supplementary Figure 11. SEM imaging of HFM1 shell surface

A) Overview (46x) of HFM1 fiber shell surface imaged by SEM after sputter coating with 5nm platinum. Red box indicates approximate location of higher zoom in next panel. B) Low-magnification (800x) shell surface view. Red box indicates approximate location of higher zoom in next panel. C) High magnification (12000x) view of the shell surface showing pore openings. Labeled distances are the shortest straight line distance across the pore indicated by yellow lines.



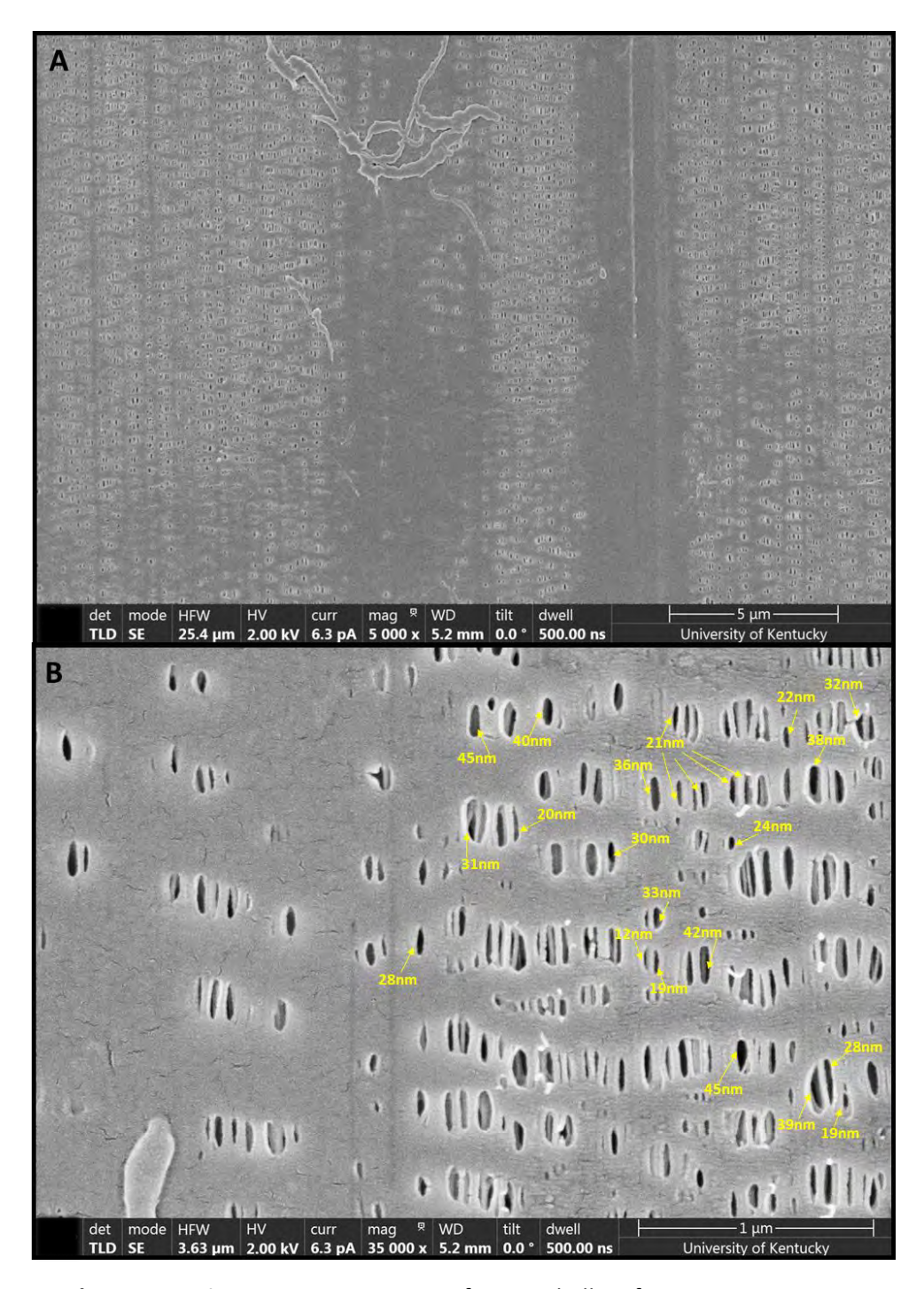
Supplementary Figure 12. SEM imaging of HFM1 cross section

A) Overview (46x) of HFM1 fiber cross section prepared by LN2 snap-freezing followed by razor cutting, followed by sputter coating with 5nm platinum. Yellow lines with labels show measured membrane thickness. Red box indicates approximate location of higher zoom in next panel. B) Low-magnification (1480x) cross section view of the same sample imaged by SEM. Red box indicates approximate location of higher zoom in next panel. C) Higher-magnification (25000x) view of the fiber outer layer showing tight pore structure. Labeled distances are the shortest straight line distance across the pore indicated by yellow lines. D) Low-magnification (650x) view of cross section prepared by ion-milling and coated in platinum, showing the transition from the tighter outer layer to the spongy region of HFM1 fiber. Red lines are labeled with measured distances across pores in red text for visibility on the light background of image.



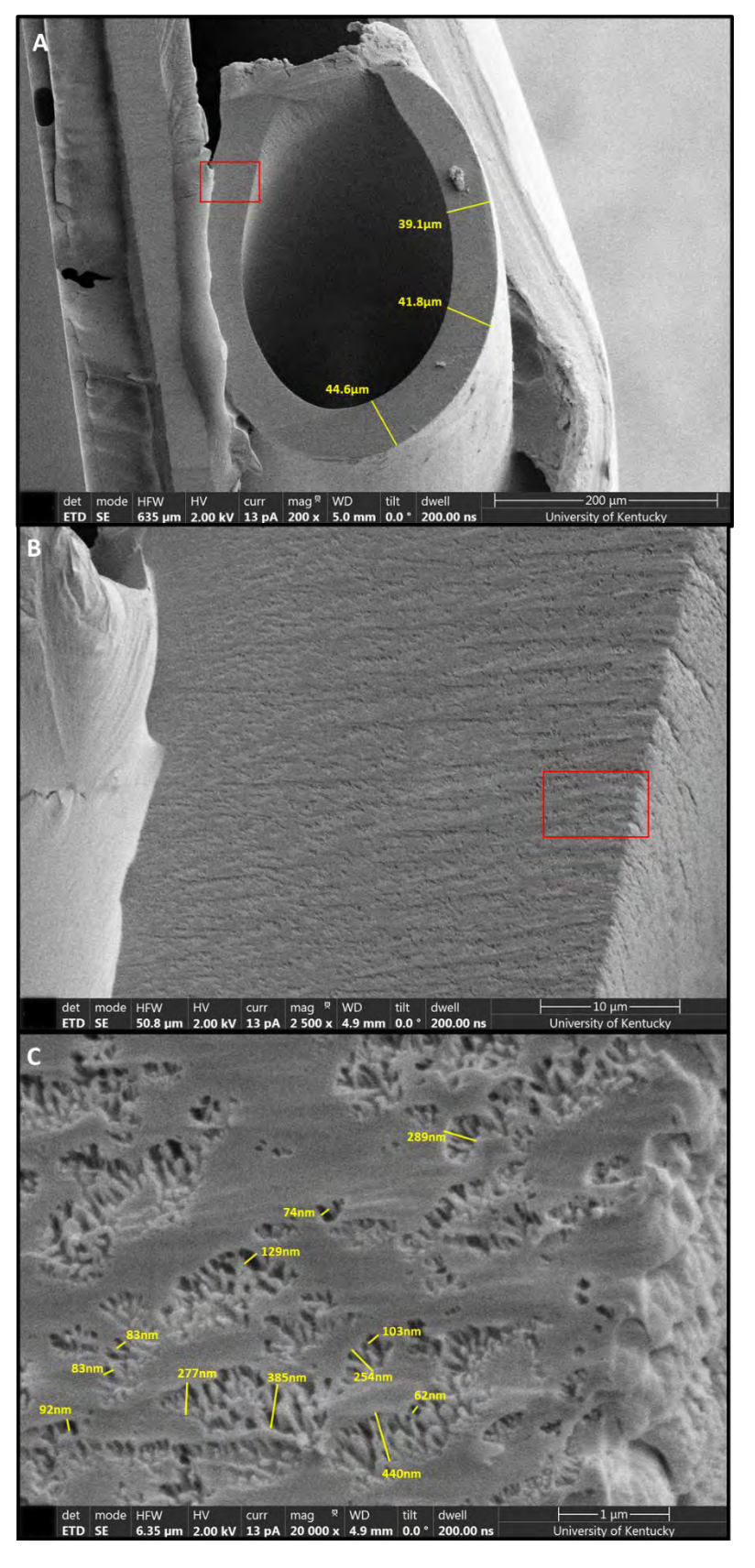
Supplementary Figure 13. SEM imaging of HFM1 lumen surface

A) Overview (43x) of HFM1 fiber lumen prepared by cutting axially with surgical scissors, without any sputtercoating. Red box indicates approximate location of higher zoom in next panel. B) Lowmagnification (500x) lumen surface view. Red box indicates approximate location of higher zoom in next panel. Labeled distances are the shortest straight line distance across the pore indicated by yellow lines. **C**) Medium-magnification (5000x) view of the fiber outer layer showing tight pore structure. Labeled distances are the shortest straight line distance across the pore indicated by yellow lines.



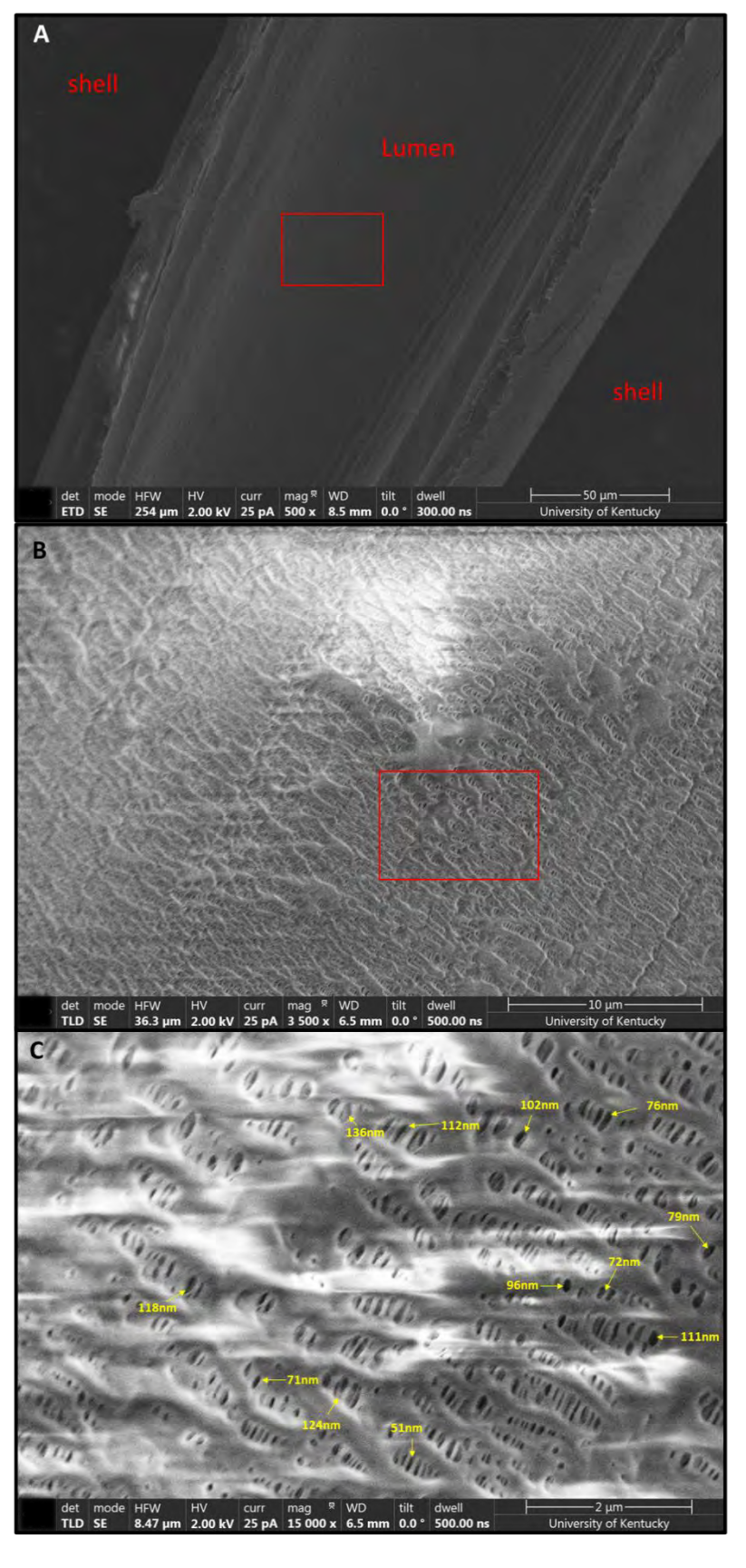
Supplementary Figure 14. SEM imaging of HFM2 shell surface

A) Low-magnification (5000x) surface view from the shell side of HFM2 hollow fiber membrane by scanning electron microscopy (FEI Helios) after sputter coating in 5nm platinum. **B)** High-magnification (35000x) surface view from shell side of HFM2. Labeled distances are the shortest straight line distance across the pore indicated by arrow.



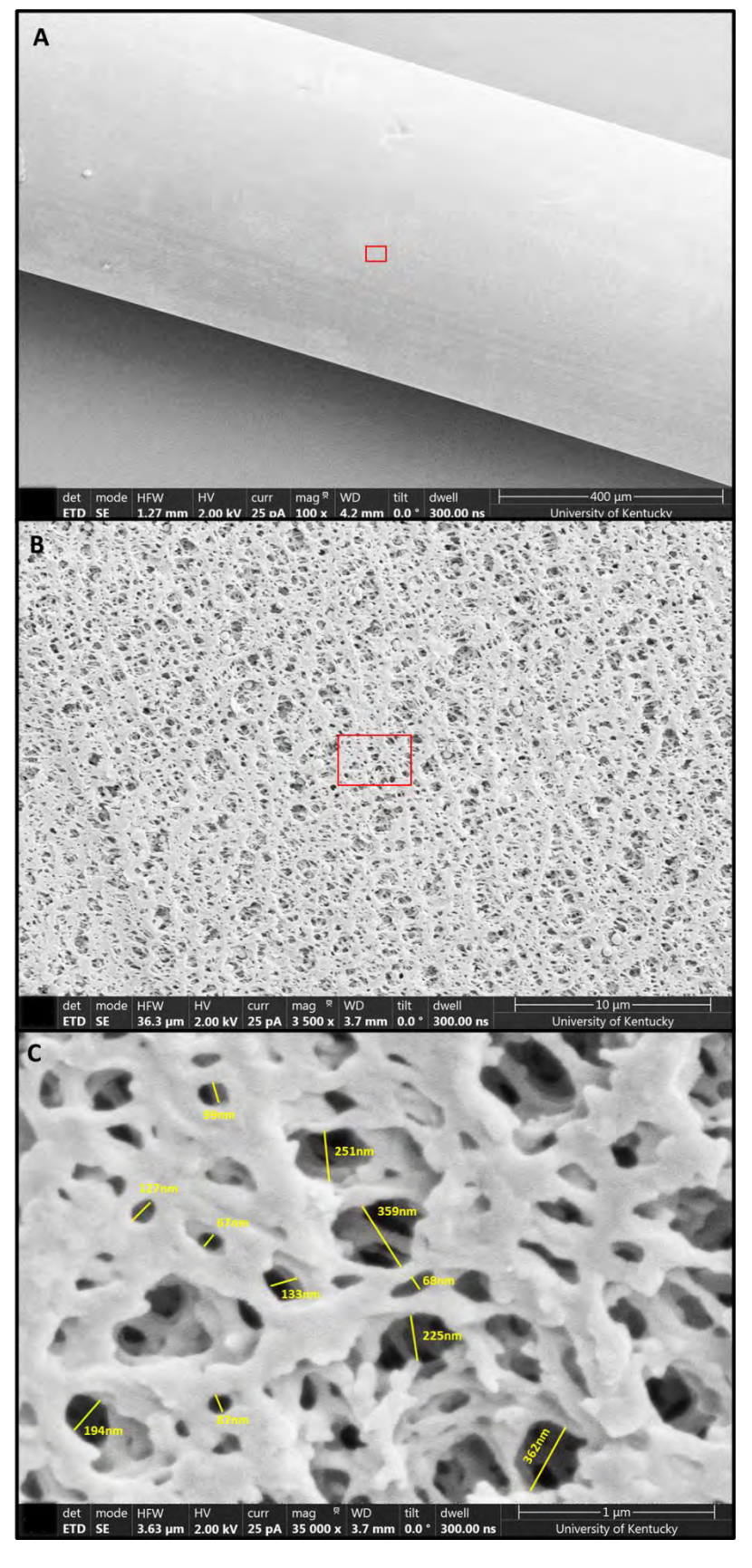
Supplementary Figure 15. SEM imaging of HFM2 cross section

A) Low-magnification (200x) crosssection view of HFM2 by scanning electron microscopy (FEI Helios) after sputter coating in 5nm platinum. Yellow lines/labels show the membrane thickness measured in Fiji. Red box indicates approximate location of higher zoom in next panel. B) Lowmagnification (2500x) cross section view of HFM2. Red box indicates approximate location of higher zoom in next panel C) Highmagnification (20000x) cross section view near the lumen surface. Yellow lines used for measurement of structural features are labeled with the line distance.



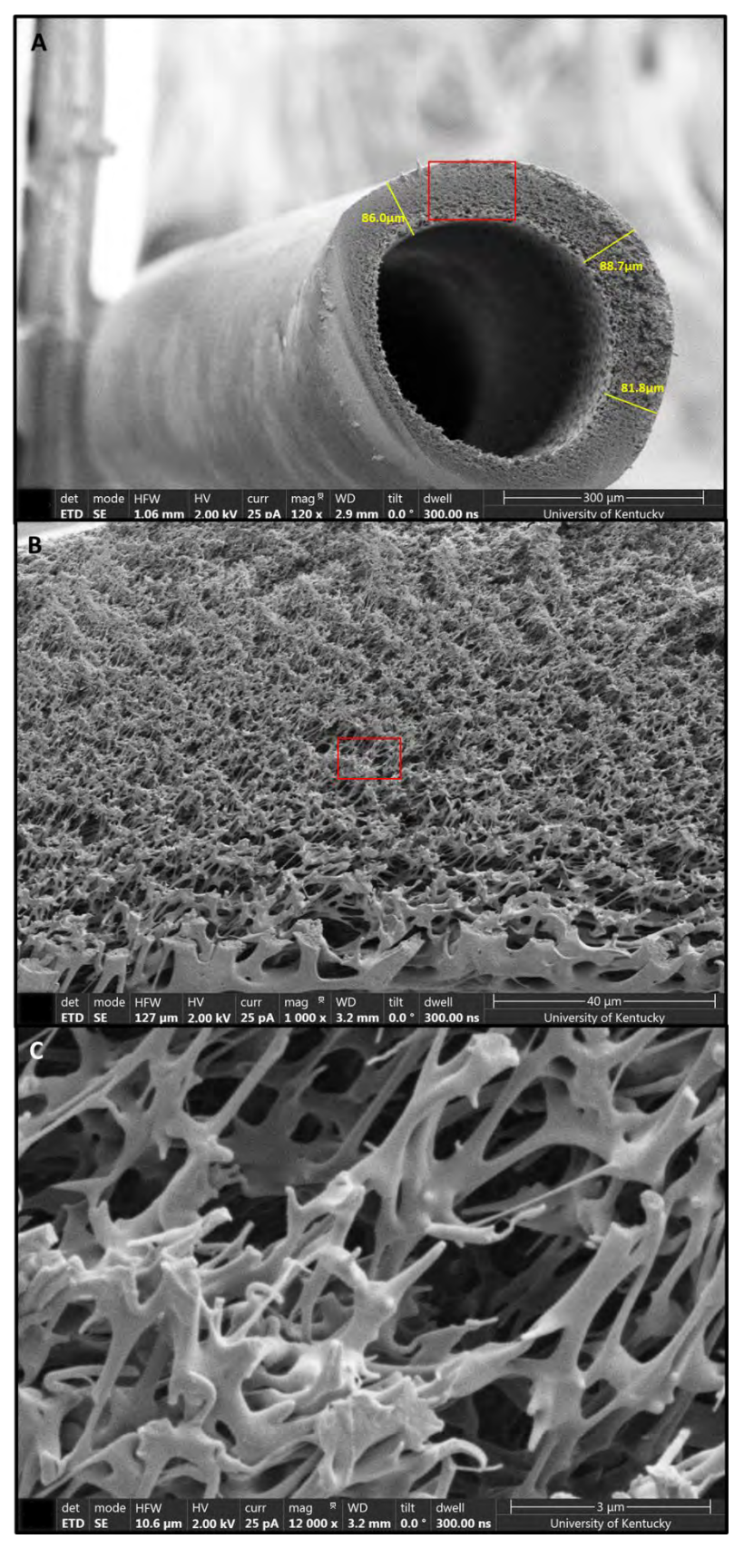
Supplementary Figure 16. SEM imaging of HFM2 lumen surface

A) Overview (500x) of HFM2 fiber cut by surgical scissors to image lumen surface. Red box indicates approximate location of higher zoom in next panel. B) Lowmagnification (3500x) surface view from the lumen side of HFM2 hollow fiber membrane by scanning electron microscopy (FEI Helios). Red box indicates approximate location of higher zoom in next panel. **C)** Higher-magnification (15000x) surface view from lumen side of HFM2. Labeled distances are the shortest straight line distance across the pore indicated by arrow.



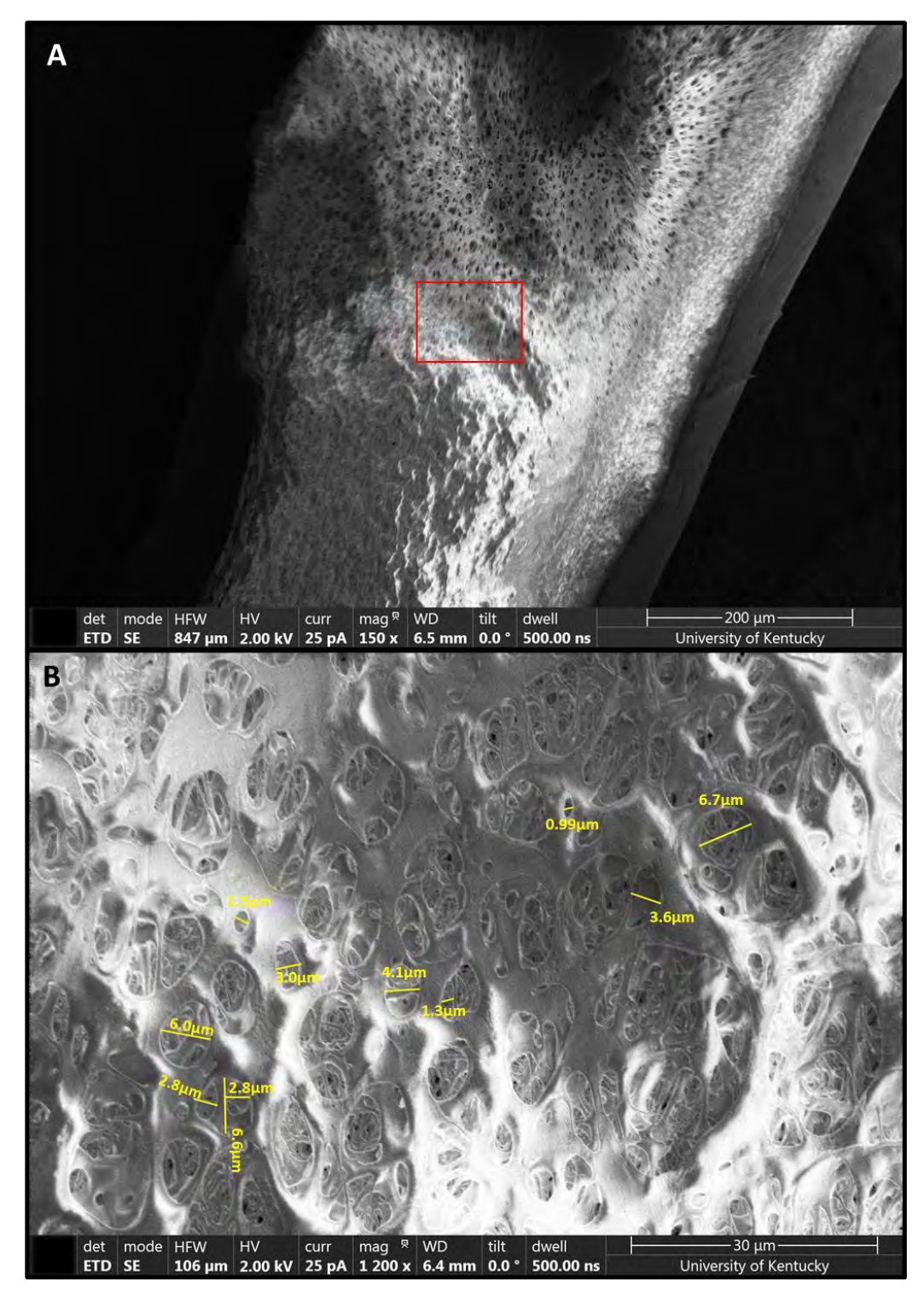
Supplementary Figure 17. SEM imaging of HFM3 shell surface

A) Low-magnification (100x) surface view from the shell side of HFM3 hollow fiber membrane by scanning electron microscopy (FEI Helios) after sputter coating in 5nm platinum. Red box indicates approximate location of higher zoom in next panel. B) Low-magnification (3500x) view of shell surface. Red box indicates approximate location of higher zoom in next panel. C) High-magnification (35000x) surface view from shell side of HFM3.



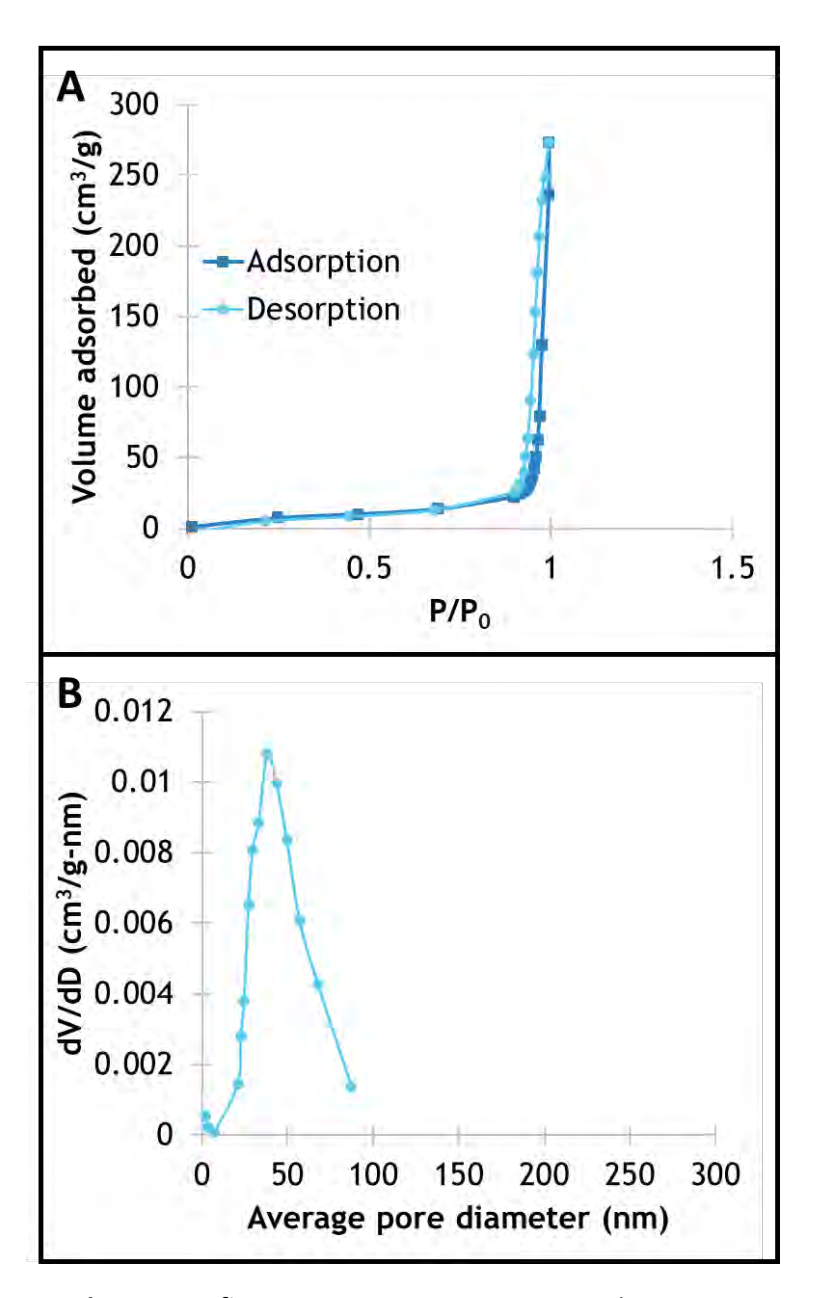
Supplementary Figure 18. SEM imaging of HFM3 cross section

A) Low-magnification (120x) cross section of HFM3 prepared by cutting with razor at room temperature, imaged by scanning electron microscopy (FEI Helios) after sputter coating in 5nm platinum. Yellow labeled lines indicated measured membrane thickness. Red box indicates approximate location of higher zoom in next panel. B) Lowmagnification (1000x) cross section view. Red box indicates approximate location of higher zoom in next panel. C) Highmagnification (12000x) crosssection view from shell side of HFM3 fiber.



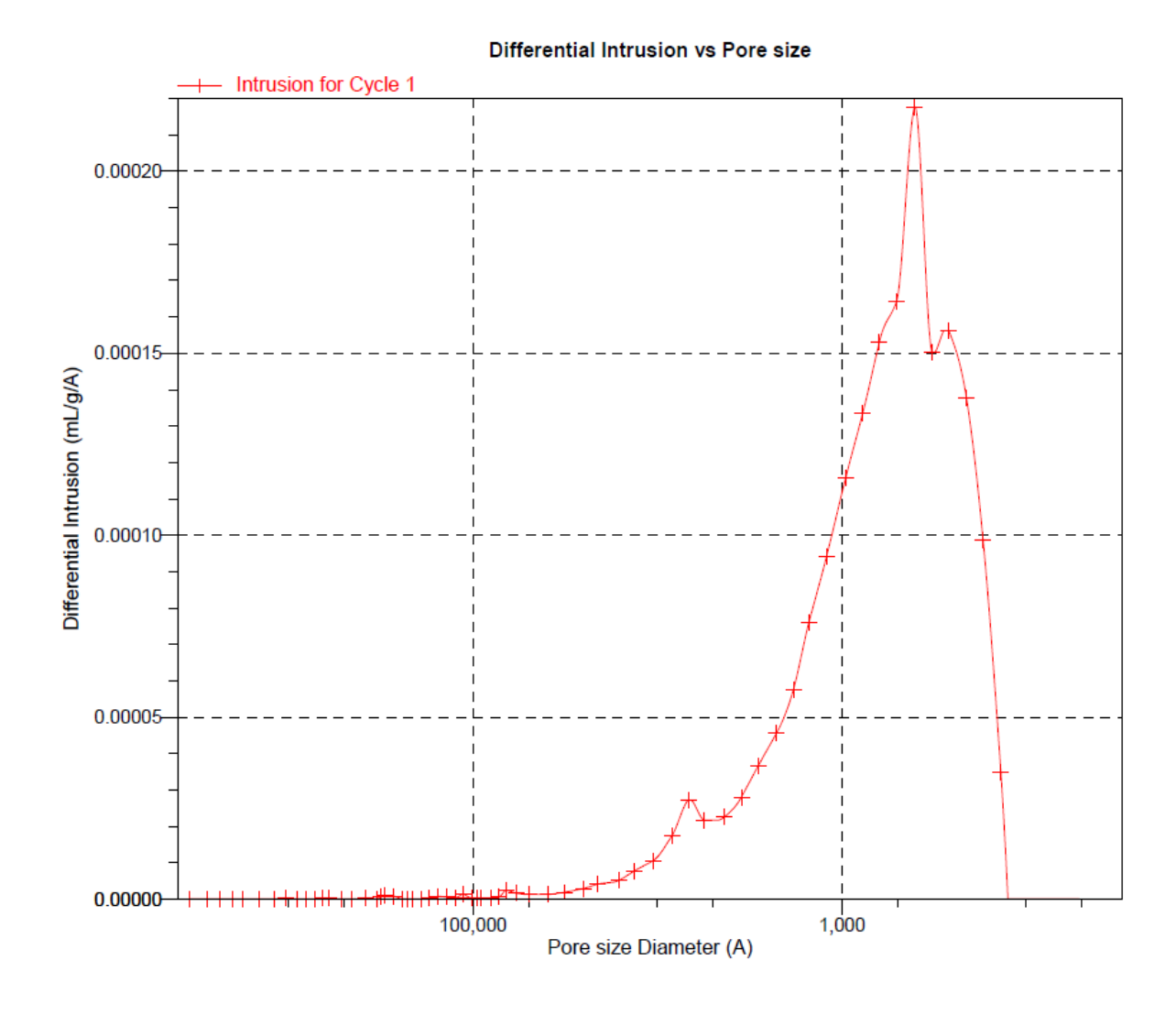
Supplementary Figure 19. SEM imaging of HFM3 lumen surface

A) Low-magnification (150x) surface view from the lumen side of HFM3 hollow fiber membrane by scanning electron microscopy (FEI Helios) after cutting axially with surgical scissors, without any sputter coating. Red box indicates approximate location of higher zoom in next panel. **B)** Low-magnification (1200x) view of lumen surface.



Supplementary figure 20. Nitrogen porosimetry characterization of HFM2 fibers

A) Nitrogen adsorption and desorption isotherms for HFM2 fibers. The hysteresis loop shape is consistent with condensation as expected with pore sizes >50nm. Furthermore, the sharp increase in volume adsorbed suggests a narrow pore size distribution. **B)** Pore sizes were calculated by the Tristar software using the BJH model from the desorption isotherm. The average pore size is as expected around 40nm, with a relatively narrow distribution.

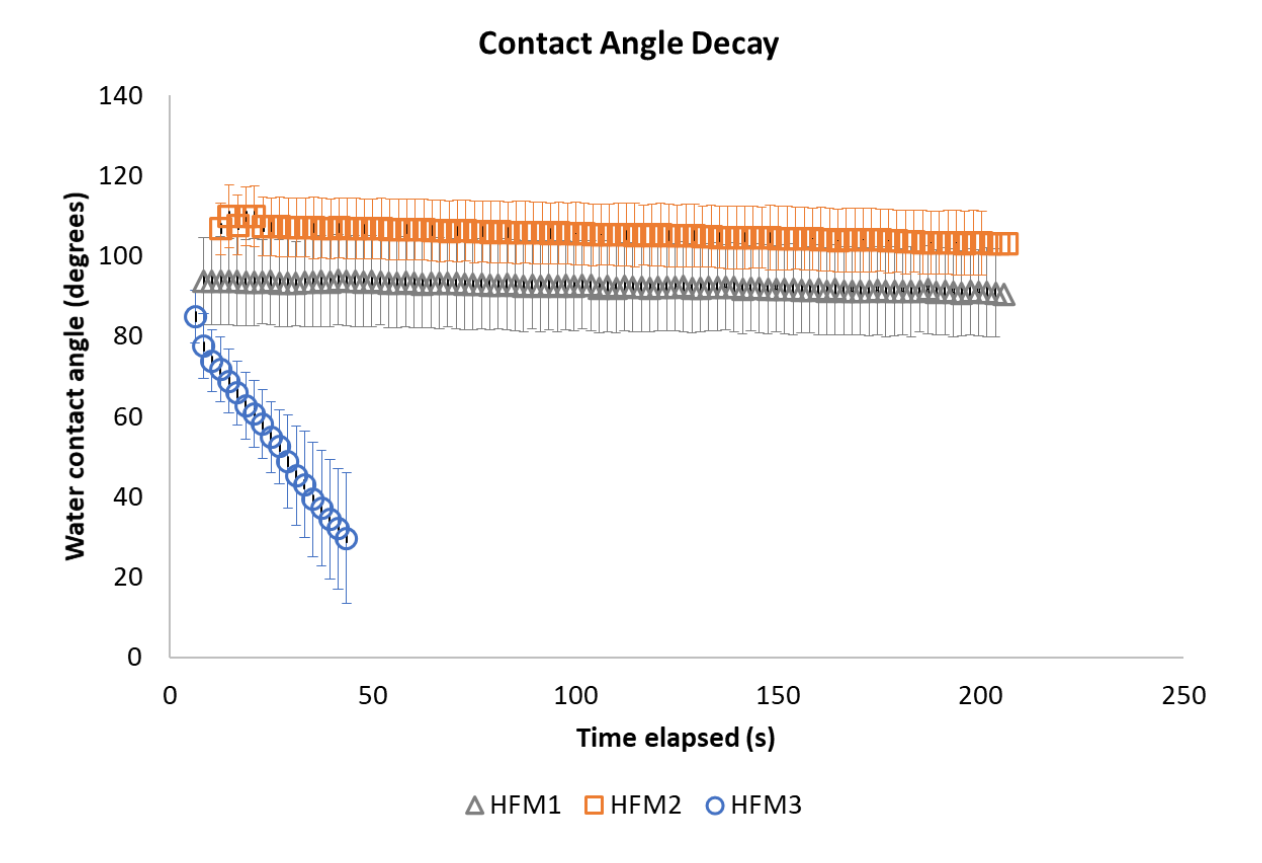


Supplementary Figure 21. Mercury porosimetry data provided by START Centre

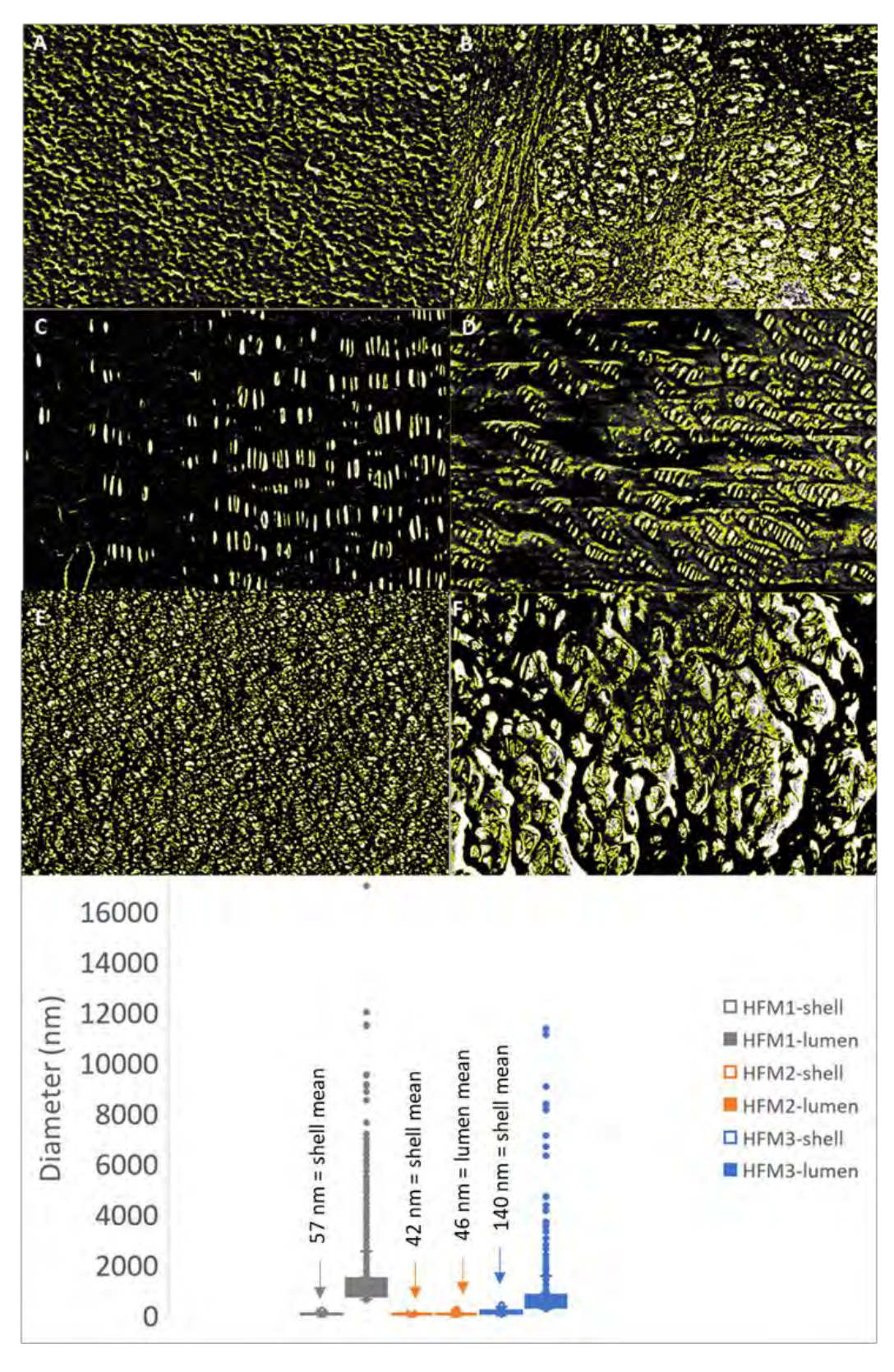


Supplementary Figure 22. Disassembled HFM modules used in this work

A) the HFM1 module was not disassembled itself, but loose fibers are shown here for comparison. The HFM1 module has some slack in the fibers similar to HFM3, however, in this module a cross-flow configuration is possible since the fiber lumen is open to a separate inlet on each end with two module inlets accessible to the shell side. B) The disassembled HFM2 module shows a unique construction, with hollow fibers woven together into a mat for rolling and packing into the module housing. This arrangement allows high density packing and also helps maintain the fibers in a straight, well ordered manner without any freedom of motion within the housing. C) The HFM3 module is arranged with both ends of the fiber open to one inlet, limiting the design to dead-end flow (no cross-flow option). The module has a plastic netting that helps keep fibers from dangling too loosely, but this module has plenty of slack in the fibers within the housing



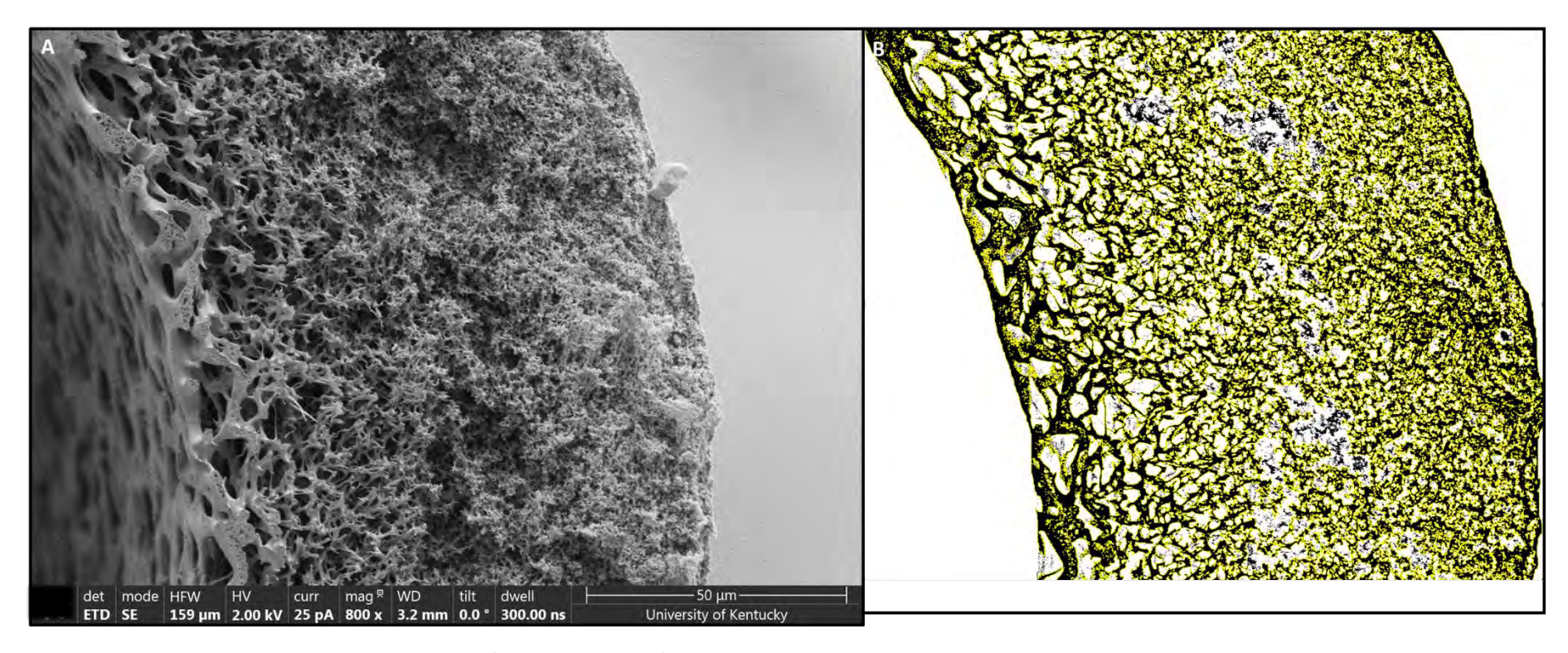
Supplementary Figure 23. Water contact angle over time for each material



Supplementary Figure 24. SEM image analysis for pore size asymmetry

Supplementary Figure 24. SEM image analysis for pore size asymmetry

Thresholded images with pore areas overlaid in yellow, matched with various images shown in supplementary figures 11-19 (refer to the original images in *previous supplementary figures for scale bars*). For HFM1, the shell (**A**) and lumen (**B**) surfaces demonstrate significant asymmetry. For HFM2, the shell (**C**) and lumen (**D**) surfaces show high similarity demonstrating symmetric pore structure. For HFM3, the shell (**E**) and lumen (**F**) surfaces show moderate asymmetry. Finally, the box plot in (**G**) shows the summarized pore size distribution (circular-equivalent pore diameter) for each example as a boxand-whisker plot



Supplementary Figure 25. SEM image analysis for bulk porosity for HFM3

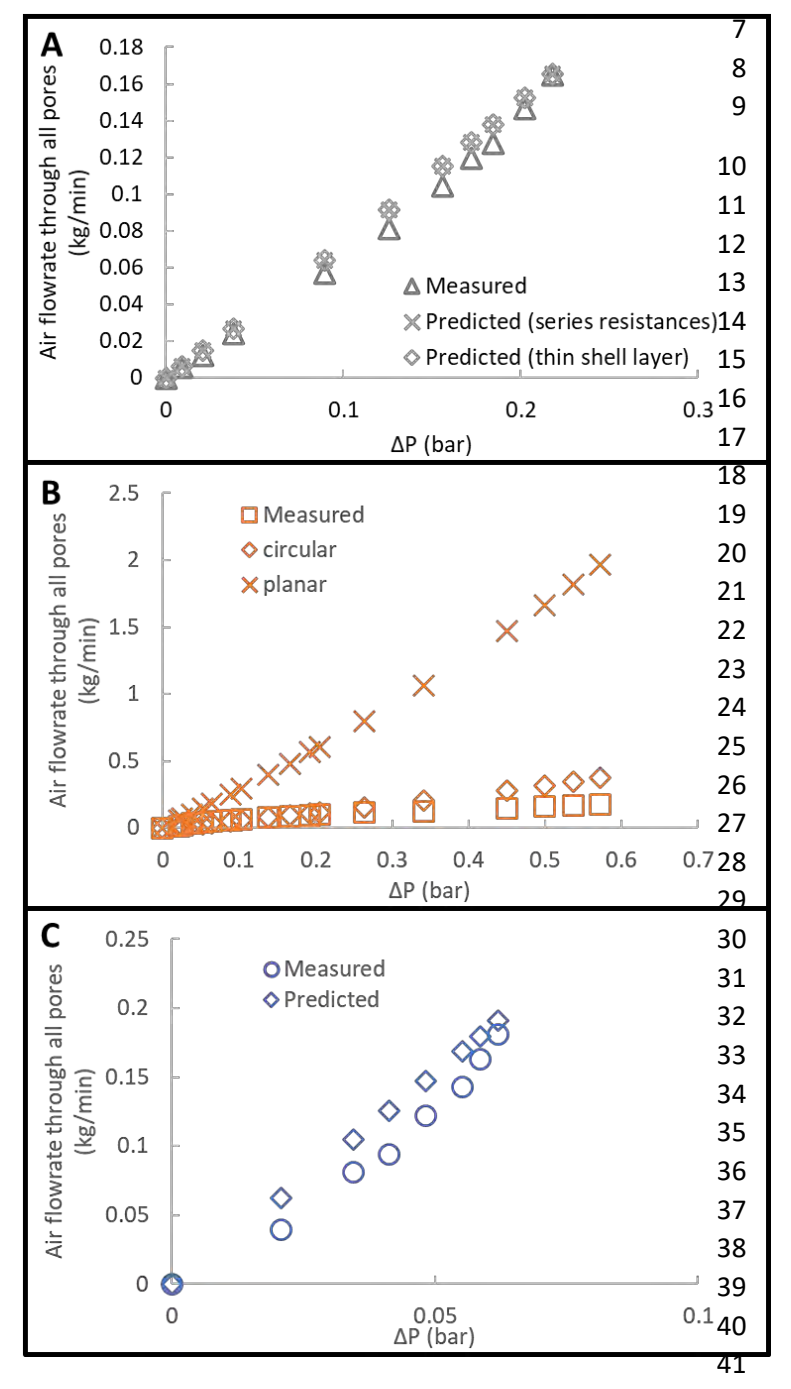
- 3 The thresholded image of HFM3 cross-section shows the pore regions overlaid in yellow. This image was used for estimating bulk porosity for
- 4 the HFM3 given the lack of direct porosimetry measurements

2

5

43

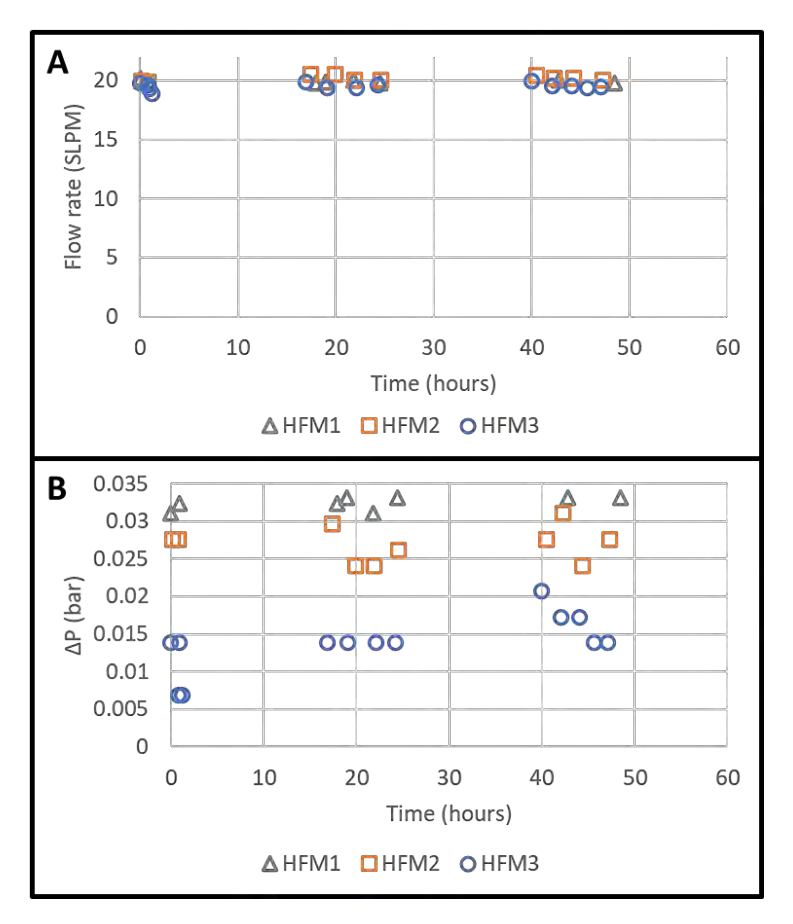
44



Supplementary Figure 26. Theoretical predictions of air flow through membranes in this work

A) Prediction of air flow through HFM1 compared to measured values. The prediction incorporating a resistancein-series framework overlaps the prediction which only uses the thin shell layer parameters, demonstrating that consideration of the most limiting membrane region is adequate for prediction of flux for highly asymmetric membranes. Porosity for these predictions was taken as 24%, from the porosimetry data provided by START Centre. **B**) prediction of air flow through HFM2 compared to measured values. The model for planar flow was also examined in this case, given that the pores are quite elliptical and may represent more of a planar flow regime; however, the circular pore equations shown in supplementary materials here predict far better, suggesting that the circular pore equations are adequate for most polymer membranes with circular or elliptical pores. Porosity for these predictions was taken as 24%, from the N2 porosimetry performed in this work, and an elliptical cross section was used for converting porosity to total pores for both circular and planar form predictions shown here. C) prediction of air flow through HFM3

compared to measured values. The porosity used for this prediction was derived from a semi-automated SEM analysis of porosity from cross section imaging (see Supplementary Figure 25), and taken as 45%.



Supplementary Figure 27. Characterization of flow **(A)** and pressure drop **(B)** across HFMs over the course of long-term two-day filtration experiment

Supplementary detailed methods

51 Interested readers are welcome to contact the corresponding author for more detailed protocols used

52 in this work.

50

53 54

55

56

57

58

59

60

61

62

63

64

65

66

67

68

69

70

71

72

73

74

75

Detailed pseudovirus aerosol filtration experiment methods

Pseudovirus stocks were thawed and diluted 1:2 into DMEM media and then placed on ice for transport from one building to the other. The bypass tubing (no HFM) was installed to determine needle valve settings. The dry air flow needle valve was set to yield a flow rate of 15 SLPM, which had previously been chosen to target a relative humidity of 40-45%, and the needle valve position was noted and used for all subsequent filtration and control tests. The pseudovirus stock was loaded into a syringe and the pump was set for 0.1 mL/min, consistent with the expected feed rate for the atomizer in recirculation mode that was used for non-biological filtration tests. The HFM test module was placed in the system, and the bubbling collection was prepared by connecting the air outlet to a serological pipette (with cotton plug removed) whose tip was submerged in 5 mL of DMEM in a cell culture flask. Finally, both dry air and atomizer air supplies were turned on, and the syringe pump was started to initiate the experiment. After 5 min, (delivery of 0.5 mL of pseudovirus solution) the pump turned off and the air supplies were left on for 1-2 min to flush remaining aerosolized viruses through the filter and system, then the air supplies were also turned off. The flask with bubbling collection was covered and set aside while the remaining HFMs and unfiltered control tests were performed. The HFM test module was then exchanged for the next test module, a new bubbling collection flask was prepared, and the process was repeated. Finally, the unfiltered control was collected by the same method, except a piece of PTFE tubing of equivalent length was used in place of any HFM test module. Then, all liquid was retrieved from each collection flask, transferred into 100kDa MWCO centrifugal ultrafiltration cassettes (Pall or Amicon), and placed back on ice for transport back to the cell culture facility. Volume of collection liquid was noted and then samples were concentrated by centrifugation at 3260g and 4°C for 4 minutes. Pseudovirus titer assays were performed from each sample, and 100 μL of sample were frozen at -80°C for later quantitative PCR analysis.

76

77

78 79

80

81

82

83

84

85

86 87

88

89

90

SEM sample preparation

HFM1

The HFM1 fibers were prepared for SEM several ways:

- Shell surface views (Supplementary Figure 9) were prepared by cutting a small piece of the fiber at room temperature with razor, followed by mounting on conductive carbon tape (Nisshin) on a standard SEM sample holder. The mounted sample was then sputter-coated with 5nm platinum (Leica EM ACE600) for subsequent imaging by SEM (FEI Helios).
- Cross section views (Supplementary Figure 10) were prepared in two ways.
 - Panel A, B, and C: Fiber sample was frozen in liquid nitrogen and fractured using a razor, mounted on conductive carbon tape using a 90° sample holder for SEM, and sputter coated with 5nm platinum.
 - Panel D: Fiber sample was cut using a razor blade at room temperature, and was then mounted on a silicon wafer with copper tape for cross section polishing by an argon-ionbeam cross section polisher (Jeol cooling cross section polisher IB-19520CCP) with

- settings of 4.0 kV, 5.0 Ar gas, -120°C using a cycle of 40s/20s on/off for total 8 hours with stage swing enabled. The polished sample with copper tape and silicon wafer was then mounted on conductive carbon tape using a 90° sample holder for SEM, and sputter coated with 5nm platinum.
 - Lumen surface views (Supplementary Figure 11) were prepared by cutting a small piece of the fiber with room temperature razor, followed by cutting axially with scissors to expose the lumen. The sample was then mounted on conductive carbon tape on a standard SEM sample holder and imaged without sputter coating.

HFM2

- Shell surface views (Supplementary Figure 12) were prepared by cutting a small piece of the fiber at room temperature with razor, followed by mounting on conductive carbon tape (Nisshin) on a standard SEM sample holder. The mounted sample was then sputter-coated with 5nm platinum (Leica EM ACE600) for subsequent imaging by SEM (FEI Helios).
- Cross section views (Supplementary Figure 13) were prepared in two ways.
 - o Panel A, B, and C: Fiber sample was cut using a razor blade at room temperature, and was then mounted on a silicon wafer with copper tape for cross section polishing by an argon-ion-beam cross section polisher (Jeol cooling cross section polisher IB-19520CCP) with settings of 4.0 kV, 5.0 Ar gas, -120°C using a cycle of 40s/20s on/off for total 8 hours with stage swing enabled. The polished sample with copper tape and silicon wafer was then mounted on conductive carbon tape using a 90° sample holder for SEM, and sputter coated with 5nm platinum.
- Lumen surface views (Supplementary Figure 14) were prepared by cutting a small piece of the
 fiber with room temperature razor, followed by cutting axially with scissors to expose the
 lumen. The sample was then mounted on conductive carbon tape on a standard SEM sample
 holder and imaged without sputter coating.

HFM3

- Shell surface views (Supplementary Figure 15) were prepared by cutting a small piece of the fiber at room temperature with razor, followed by mounting on conductive carbon tape (Nisshin) on a standard SEM sample holder. The mounted sample was then sputter-coated with 5nm platinum (Leica EM ACE600) for subsequent imaging by SEM (FEI Helios).
- Cross section views (Supplementary Figure 16, 23) were prepared in two ways.
 - Panel A, B, and C: Fiber sample was cut using a razor blade at room temperature, mounted on conductive carbon tape using a 90° sample holder for SEM, and sputter coated with 5nm platinum.
- Lumen surface views (Supplementary Figure 17) were prepared by cutting a small piece of the fiber with room temperature razor, followed by cutting axially with scissors to expose the lumen. The sample was then mounted on conductive carbon tape on a standard SEM sample holder and imaged without sputter coating.

- 130 Air permeability characterization
- 131 Total module area estimation
- 132 For the HFM2 module, electron microscopy was used to measure spacing between fibers in the mat, and
- the total length of the fiber mat was estimated as an archimaedian spiral to determine total surface area
- in the module. For the HFM3 module and the HFM1 module, the fiber length and diameters were
- measured using a ruler and phone camera, then image analysis was used to extract fiber dimensions and
- 136 counts for total area determination.
- 137 Pressure drop correction
- 138 For HFM1 and HFM2, a pressure drop correction was applied based on experimental characterization of
- pressure drop in different flow modes. Specifically, the shell-side luer-lok fittings for HFM2 contribute
- significantly to measured pressure drop, and HFM2 has longer fibers that contribute significantly to the
- measured pressure drop. As such, the HFM1 pressure drop measurements were corrected by first fitting
- a quadratic regression to the pressure drop measured for shell-shell flow configuration (i.e. not passing
- through the membrane)

156

162

- 144 Derivation of circular pore flow from Zohar et al model
- 145 We begin from equation 32 in Zohar et al, which gives the leading order perturbation solution for mass
- 146 flow rate $(Q^{(0)})$ through a microchannel:
- 148 $Q^{(0)} = \frac{1 + (3+m)2Kn}{(m+1)^2(m+3)} (2-m)(2\pi)^m D^{(1-m)} H^{(3+m)} \frac{X}{\mu L}$ (S1)
- where Kn, D, H, μ, and L are the Knudsen number, pore height, pore half-width or radius, viscosity, and
- pore length, respectively. The variable m is an index variable denoting pore shape, with m=1
- 151 corresponding to a circular pore and m=0 corresponding to a planar pore (the derivation of which is
- carried out by Zohar. In the previous equation S1, the variable X represents a parameter accounting for
- 153 fluid compressibility (see Zohar et al equation 11). In order to derive the equation for a circular pore, we
- substitute m=1 into equation S1:

$$Q^{(0)} = \frac{1+8Kn}{16} 2\pi H^4 \frac{X}{\mu L} \tag{S2}$$

157 From equation S2, we substitute the derived parameter X from Zohar et al equation 11:

158
$$Q^{(0)} = \frac{1+8Kn}{16} 2\pi H^4 \frac{\langle \rho(P)\Delta P \rangle}{\mu L}$$
 (S3)

159 And substituting the average density of the compressible fluid from the ideal gas law given the average

pressure across the pore length, we obtain the following

$$Q^{(0)} = \frac{1+8Kn}{16} 2\pi H^4 \frac{1}{\mu L} \left(\Delta P \frac{P_o}{RT} \frac{P_i + P_o}{2P_o} \right)$$
 (S4)

From equation S3, we rearrange to obtain a similar form as the final solution given by Zohar et al (equation 58 in their work) for the planar microchannel:

$$Q^{(0)} = \left(\frac{\pi H^4}{8\mu L} \Delta P \frac{P_o}{RT}\right) \left(\frac{P_i + P_o}{2P_o}\right) (1 + 8Kn) = Q_i \alpha_C \alpha_S \tag{S5}$$

- where $\left(\frac{\pi H^4}{8\mu L}\Delta P\frac{P_o}{RT}\right)$ is the incompressible mass flow rate (Q_i), $\left(\frac{P_i+P_o}{2P_o}\right)$ is the compressibility correction
- factor (α_c), and (1 + 8Kn) is the slip correction factor (α_s). Equation S5 gives the leading order
- approximation of mass flow rate for a compressible fluid through a circular microchannel/pore
- accounting for fluid compressibility and slip flow.
- 170 Assuming that the incompressible flow rate can be approximated by poiseuille's law, that is

$$Q_i \propto \frac{\Delta P}{R} \tag{S6}$$

- where R is the total resistance to flow. By rearranging equation S5, we can determine the formula for
- 173 resistance in this model:

$$Q_i = \left(\frac{\pi H^4}{8\mu L} \Delta P \frac{P_o}{RT}\right) = \Delta P \left(\frac{\pi H^4}{8\mu L} \frac{P_o}{RT}\right) = \frac{\Delta P}{8\mu LRT} / \pi H^4 P_o$$
 (S7)

$$R = \frac{8\mu LRT}{\pi H^4 P_O} \tag{S8}$$

- In considering then an asymmetric pore with two sections, m (smaller pore) and n (larger pore),
- application of poiseuille's law approach for total incompressible flow and applying the previously
- determined compressibility and slip flow correction factors (assuming pressure drop across the region n
- is not significant, i.e. Po factor in both resistance formulae are the same):

180
$$Q^{(0)} = \frac{\Delta P}{R_m + R_n} \left(\frac{P_i + P_o}{2P_o}\right) (1 + 8Kn) \tag{S9}$$

181
$$Q^{(0)} = \frac{\Delta P}{\frac{8\mu L_m RT}{\pi H_m^4 P_o} + \frac{8\mu L_n RT}{\pi H_n^4 P_o}} \left(\frac{P_i + P_o}{2P_o}\right) (1 + 8Kn)$$
 (S10)

- 182 Comparison with HEPA for air handling calculations
- 183 A small restaurant total volume was estimate by the following equation:

184
$$V_{restaurant} = 20m \times 10m \times 2.5m = 500m^3$$
 (S11)

185 The time to change over a full volume of air is calculated by the following equation:

$$t_{1x \ air \ change} = \frac{V_{restaurant}}{Q_{Filter}}$$
 (S12)

- 187 In the case of HFM3, the slope (m) and intercept (b) were taken from the data in Figure 3 and used to
- 188 calculate flow rate:

189
$$Q_{HFM3} = (m_{HFM3} \times 0.5 \ bar - b_{HFM3}) \times \frac{m^3}{1,225g} \times Area_{HFM3}$$
 (S13)

For HEPA filters, the air processing capacity was taken as the minimum specifications for FC 1 HEPA filters (for most comparable expected cost to HFM modules) given by the Department of Energy specifications (ref 50 in main text):

$$Q_{HEPA} = 42 \frac{m^3}{h}$$
 (S14)

194 SEM pore size and porosity analysis

195 Surface pore size distribution analysis

Image analysis was performed via semi-automated procedures using Fiji (ImageJ). Automatic local thresholding was performed using the Phansalkar algorithm with the radius chosen manually for each image to optimize the thresholded binarization for closest match to the original image. The particle analyzer tool was then employed (in most cases, default particle size limit ranges were used, with manual adjustments in some cases) to identify pores as "particles". The resulting thresholded images with identified particles annotated in yellow are shown in Supplementary Figure 22, along with box plots representing the pore size distributions derived from each image.

Overall porosity analysis for HFM3

A similar semi-automated particle analysis procedure was followed for the overall porosity of HFM3, using a cross-sectional SEM image in this case. The thresholded image with identified pores annotated in yellow is shown in Supplementary Figure 23. The sum of all identified pore areas was divided by the total membrane area (i.e. ignoring large white spaces at right and left of image) in the image and multiplied by 100 to obtain the porosity value presented in Table 1 as a percentage value (see below equation S11)

210
$$Porosity \% = \frac{\sum_{i} A_{pore,i}}{A_{total}} \times 100$$
 (S11)

Contact angle measurements

For contact angle measurements, a loose fiber for each of HFM1, HFM2, and HFM3, were dried in a vacuum oven (~70kPa vacuum at ~40C) for 2.5 hours. After drying, each was then cut into small pieces, and the pieces were laid out side by side on a glass slide with double sided tape. Then a clean polypropylene pipette tip was rolled over each to flatten the fibers into a flat sheet for contact angle analysis. Contact angle decay analysis was then carried out using an automated procedure consisting of 5 minutes of imaging with contact angles measured every 2 seconds. The automated procedure was started, and within the first 10 seconds, a 2uL drop of Type I deionized water was placed manually on the flattened sheet of hollow fibers and analyzed by the automated procedure. This process was repeated in three locations on each flattened sheet of hollow fibers from each membrane (HFM1, HFM2, HFM3).

Synthetic nanoparticle protein labeling detailed methods

Labeling of 100nm PSL-COOH (carboxyl-functionalized polystyrene latex, Bangs Laboratories) was performed by first labeling particles with Ni+ followed by 6x-HisTag affinity capture of superfolder GFP (gift from Yinan Wei lab in UK Dept. of Chemistry) or SARS-CoV-2 spike protein produced in E. coli (Thermo Fisher Scientific). PSL-COOH suspensions at 10.2% solids were washed twice by 15x dilution

into DI water and centrifugal ultrafiltration (10kDa MWCO, Amicon) to reconcentrate to ~1x volume. Next, the nanoparticles were diluted 15x into 10mM NiCl2-6H2O (Sigma Aldrich) with one hour incubation at room temperature with occasional mixing by inversion to bind nickel to the COOH nanoparticle surface, followed by reconcentration and 2-3 additional washes in DI water using the same centrifugal UF cassette. Protein labeling was achieved by diluting PSL-COOH+Ni+ into 15x volume of superfolder GFP-6xHis at ~500 nM in 1x PBS (pH=8.1) with 1-2 hr incubation at room temperature with occasional agitation. The protein labeled nanoparticles (PSL-sfGFP) were then washed three times in 15x volume of 1xPBS pH=8.0 as previously described, with final dilution to ~0.7% solids in 1xPBS pH=8.1 for storage at 4°C in the dark for up to one month. The protocol for labeling with SARS-CoV-2 spike protein was the same, with 500 nM spike protein replacing the sfGFP in the binding solution. Successful protein labeling was verified by DLS, and after several weeks of storage the stability of protein labeling was verified by ultrafiltration of the nanoparticle suspension with no apparent GFP release (Supplementary Figure 3).

Stability of protein labeling was checked after approximately three months by using a microfiltration membrane (using Pall 100kDa MWCO for GFP, and ~50nm pore PVDF-400 microfiltration membrane from Solecta for spike protein) to eparate storage buffer from the labeled PSL and for separation at subsequent steps. The PSL were then eluted twice with 2mM EDTA in 1xPBS pH8.0 and then rinsed with MilliQ water, and the eluted PSL were recovered from the retentate. The labeled PSL, the storage buffer flow-through, both elutions, the water rinse, and the eluted PSL were analyzed by Bradford assay; the labeled PSL, the storage buffer flow-through, and the first elution were then analyzed by SDS-PAGE.